The Thesis committee for Rohan Ram Mahadik

Certifies that this is the approved version of the following thesis:

Harvesting wind energy using a galloping piezoelectric beam

APPROVED BY

SUPERVISING COMMITTEE:

Supervisor: _____

Jayant Sirohi

_____

Jeffrey Bennighof

Harvesting wind energy using a galloping piezoelectric beam

by

Rohan Ram Mahadik B.Tech

Thesis

Presented to the Faculty of the Graduate School

of the University of Texas at Austin

in Partial Fulfillment

of the Requirements

for the Degree of

Master of Science in Engineering

The University of Texas at Austin

May 2011

Dedicated

To My

Sister, Rucha and my Parents

Acknowledgements

I would like thank Dr.Jayant Sirohi, my advisor, for guiding me so well during the entire period of my research. He has been a mentor at every point of time in my Master's program. His criticism helped me in improving over my mistakes. His attittude towards understanding me as student, helping me come up with a solution, helped a lot. The research carried out as a part of the thesis, would not have been possible without his supportive nature and continual guidance. I realized the importance of fundamentals and the need of strong base in one's area of study while working with him. Secondly, I would like to thank my sister, Rucha, and my parents for being so supportive. I would also like to thank my friends from Bangalore, India, namely, Ghanshyam Lalwani, Pankaj Patel and Jayesh Rathod who supported me in all situations, before I joined my Master's program at University of Texas at Austin. All my friends from Austin have been truly amazing and supportive during my entire stay, with a special mention for Mithun, Tamanna, and Tushar. I would also like to acknowledge Jerome Sicard, my colleague, for being helpful in the lab, at times, during my Master's program. Special thanks to Dr. Jeffrey Bennighof for taking out time to read my thesis and give me valuable suggestions.

Harvesting wind energy using a galloping piezoelectric beam

By

Rohan Ram Mahadik, M.S.E.

The University of Texas at Austin, 2011

SUPERVISOR: Jayant Sirohi

Galloping of structures such as transmission lines and bridges is a classical aeroelastic instability that has been considered as harmful and destructive. However, there exists potential to harness useful energy from this phenomenon. The study presented in this paper focuses on harvesting wind energy that is being transferred to a galloping beam. The beam has a rigid prismatic tip body. Triangular and D-section are the two kinds of cross section of the tip body that are studied, developed and tested. Piezoelectric sheets are bonded on the top and bottom surface of elastic portion of the beam. During galloping, vibrational motion is input to the system due to aerodynamic forces acting on the tip body. This motion is converted into electrical energy by the piezoelectric (PZT) sheets. A potential application for this device is to power wireless sensor networks on outdoor structures such as bridges and buildings. The relative importance of various parameters of the system such as wind speed, material properties of the beam, electrical load, beam natural frequency and aerodynamic geometry of the

tip body is discussed. A model is developed to predict the dynamic response, voltage and power results. Experimental investigations are performed on a representative device in order to verify the accuracy of the model as well as to study the feasibility of the device. A maximum output power of 1.14 mW was measured at a wind velocity of 10.5 mph.

Contents

List of Tables

List of Figures

1. Introduction

1.1 Galloping

Galloping of a structure is characterized as a phenomenon involving low frequency, large amplitude oscillations normal to the direction of incident wind. Typically, it occurs in lightly damped structures with asymmetric cross sections. Galloping is caused by a coupling between aerodynamic forces acting on the structure and the structural deflections.

Consider a body within a fluid at rest. Let the body be a flexible structure having some stiffness. If it is excited by an impulse forcing, it will undergo oscillation but eventually, the structural damping and the viscosity of the surrounding fluid will attenuate the oscillations and the body will come to rest. However, due to interaction with fluid, there is a possibility that the body may be acted upon by forces with an appropriate phasing. An appropriate phasing would mean that the forces generated are acting at a point in the periodic cycle when they do not attenuate but enhance the disturbance caused. In such a case, the body might continue to oscillate or even amplify its oscillations. Such a behavior occurs when the body is unstable. The state of being unstable can be defined as the state when the forces act in a phasing so as to increase oscillation amplitude. This behavior is called galloping. Galloping can be called as self-excited

oscillations. It can be translational or torsional in nature. The thesis discusses translational galloping only.

Den Hartog [1] explained the phenomenon of galloping for the first time in 1934 and introduced a criterion for galloping stability. He was the first to explain how disturbances can also cause self-excited vibrations. In self-excited vibration the alternating force that sustains the motion is created or controlled by the motion itself; when the motion stops, the alternating force disappears. In an ordinary forced vibration, the sustaining alternating force exists independently of the motion and persists even when the vibratory motion is stopped. Another way of looking at this matter is by defining self-excited vibration as vibration with negative damping.
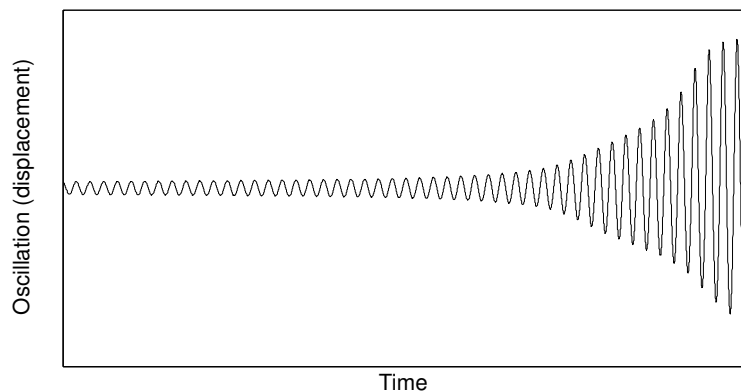
Figure 1-1: Schematic of negatively damped oscillation

A system with negative damping is dynamically unstable. The oscillations grow or magnify in amplitude with time as shown in Fig 1-1. On the other hand, a

2

system with positive damping is dynamically stable. The oscillations reduce in amplitude with time.

Den Hartog explained how self excited oscillations occur due to winds with the help of an example about galloping of ice-covered electrical transmission lines. Transmission lines have been observed to vibrate with large amplitudes during winter weather conditions. This phenomenon has been observed in cold countries like Canada and Northern part of the U.S. during winter when a strong transverse wind is blowing. The frequency of vibration has been observed to be same as the natural frequency of the transmission line system. The cross section of the transmission line cable is generally circular. Circular section being symmetric is dynamically stable if transverse wind is blowing. There is no disturbance force acting on it. However, when ice sleet is formed underneath the transmission line, the circular cross section now converts into an asymmetric shape as shown in Fig 1.2. Such asymmetric shapes are prone to exhibit galloping. Chabart and Lilian [2] have conducted galloping experiments in wind tunnel on scaled bodies to replicate galloping of transmission lines having ice-sleet on them.
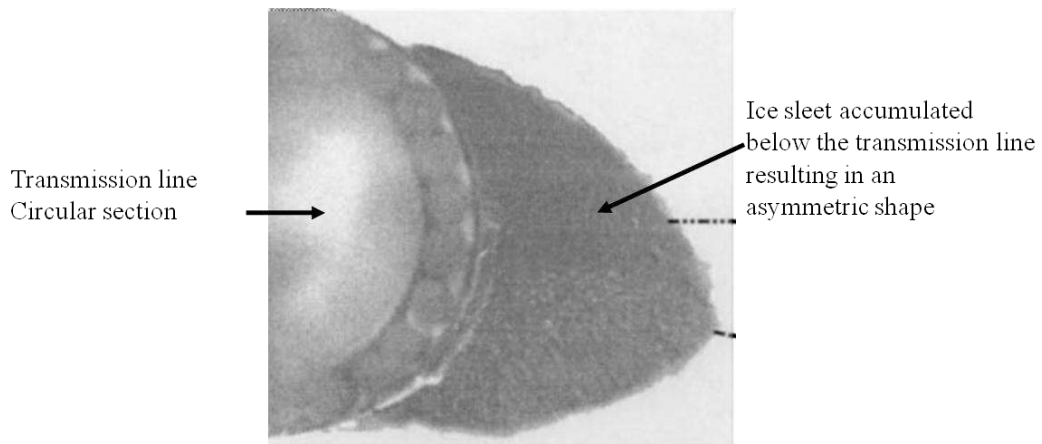
Figure 1-2: Transmission line section [2]

There are various asymmetric shapes that are prone to galloping. Studies have been carried out in past on different cross-sections, such as, rectangular, prismatic, D-section and triangular. Significant research has also been done to study various other parameters that influence galloping of structures due to wind. Alonso et al. [3] conducted experimental measurements on a triangular cross section undergoing galloping due to wind. Alonso et al. demonstrated experimentally the dependence of angle of attack[*] on occurrence of galloping. He determined aerodynamic coefficients, such as lift and drag, over a range of angle of attack from 0 to 180 degrees by means of wind tunnel experiments. This was helpful in predicting the unstable region in that range, for an isosceles triangular section subjected to transverse wind.

---

* Angle of attack: Angle between wind velocity incidence and mean chord of a section undergoing galloping at an instant of time.

4

The vertex angle of an isosceles triangular section also decides the instability. Kazakevich and Vasilenko [4] have investigated and found dependence of galloping amplitude on wind velocity by a means of a closed form analytical solution for a rectangular section. They showed galloping begins only beyond a certain wind velocity, called as critical wind velocity. It is the minimum wind velocity required to initiate galloping and varies from section to section. Using their model, critical wind velocity can be predicted for rectangular sections. They have also discussed how breadth to height ratio affects the stability of rectangular section. From this example and the previous example of isosceles triangular section, it is seen that geometry plays a significant role in galloping. Experimental results obtained by Laneville et al. [5] on a D-section exposed to wind flow show that it is highly prone to galloping at higher angles of attack. Thus, this past research identifies influence of parameters such as geometry of the section, wind velocity and angle of attack, on galloping stability.

The self-excited structural oscillations are a form of available mechanical energy. They can be beneficial if harvested into useful form. The following section discusses the concept of energy extraction, and the currently available devices that can extract energy available from different energy sources, into useful form.

1.2   Energy Harvesting

Energy harvesting is the process of converting available energy from one form to another useful form. As a part of this thesis, conversion of structural vibrations to useful electrical energy has been discussed. There are several ways to harvest energy. The methods discussed here, relevant to this study, are:

1.   Harvesting energy from base-excited vibration
2.   Harvesting energy from flow induced vibrations
3.   Harvesting energy from flutter due to wind flow

Energy harvesting from base-excited vibration is done by conversion of available ambient vibration at source into electrical energy. The source of ambient vibration, as an example, can be operating machinery. The method of conversion involves using smart materials such as piezoelectric (PZT) materials. Piezoelectricity refers to generation of electricity when such smart materials are subjected to mechanical stress. It is observed in many naturally occurring crystals. Most piezoelectric materials are crystalline in nature; they can be either single crystals or polycrystalline. The unit cell of these crystals possess a certain degree of asymmetry, leading to separation of positive and negative charges that results in permanent polarization. The effect was first predicted and then experimentally measured by the Curie brothers, Pierre and Jacques, in 1880. This effect is also

6

known as the direct piezoelectric effect which means electric polarization produced by mechanical stress, is directly proportional to the applied stress. In other words, if stress is applied to the piezoelectric material, a proportional electrical charge is produced. This charge can be extracted by means of an electrical circuit.

. Piezoelectric materials have found wide application as low power generators. In the majority of these applications, the energy harvester is attached to a structure, and it extracts energy from ambient vibrations by operating as a base-excited oscillator. Several analytical models have been proposed to quantify the electrical energy that can be generated. Sodano et al. [6] developed a model of a piezoelectric beam undergoing base-excited vibrations, to predict the dynamic response, power, voltage and current output. The model uses energy methods to develop constitutive equations for a bimorph piezoelectric energy harvesting beam. Umeda et al. [7] investigated the electrical energy generated by a metal ball falling on a plate with a bonded piezoelectric sheet, and proposed an electrical equivalent circuit that described the conversion of potential energy into electrical energy in the piezoelectric material. Roundy et al. [8] discussed the operation and analytical modeling of a base-excited energy harvester consisting of a piezoelectric bimorph with a lumped mass attached to its tip. A relationship for power output as a function of input vibration amplitude and frequency was developed. Ottman et al. [9] designed optimal power conditioning electronics for a piezoelectric generator driven by ambient vibrations. Ajitsaria et al. [10]

developed mathematical models for the voltage generated by a bimorph piezoelectric cantilever beam, using three different approaches.

Several academic research institutions and commercial manufacturers are involved in the design and manufacturing of energy harvesters excited by ambient vibration. Some of them are listed here. They include IMEC and the Holst Centre – Eindhoven Netherlands, Massachusetts Institute of Technology at Boston, Georgia Institute of Technology at Atlanta, University of California at Berkeley, Southampton University in U.K, PMG Perpetuum, and National University of Singapore.

IMEC & Holst centre [10] has developed a micro-machined energy harvester which delivers 60μW power at an input acceleration of 2g and resonance frequency equal to 500Hz. It consists of a piezoelectric capacitor formed by a Pt electrode made of an aluminium-nitride (Al-N) layer and a top Al electrode. The capacitor is fabricated on a cantilever beam which has a tip mass. When the harvester vibrates, the mass on the cantilever causes the piezoelectric layer to bend, inducing an electrical power. The Al-N layer has advantage over piezoelectric material that it can be made by a simpler deposition process. AdaptivEnergy [12] designs, manufactures and markets energy harvesting power solutions. The company provides a range of products for different operating frequencies and required output DC voltage. The product module is designed to operate at random vibration environments. In its present form and application space, the module can power microelectronic devices such as microcontrollers,

wireless switches, wireless sensor networks and ActiveRFID tags in transportation and industrial environments. Environment such as bridges, roads, tunnels, motors, compressors, pumps, helicopter and power transformers are used as vibration source by these energy harvesting modules. Advanced Cerametrics Incorporated − ACI's Harvestor line of products [13] produce electrical power from ambient vibration energy by means of piezoelectric fiber composites (PFC) and their proprietary efficient power management circuits. The working principle is that the piezo-ceramics bend due to input vibration and electrical charge is produced. Their latest power module product named 'Harvester–III' is light weight, compact in size, with different models available to operate at different excitation frequencies of vibration. Mide Technology Corporation [14], located in Cambridge, Boston, Massachusetts, is another manufacturer of wireless vibrational energy harvesters named 'Volture'. PMG Perpetuum [15] , located in Southampton, U.K., is a leading producer of vibration energy harvesting products. All the above studies targeted piezoelectric energy harvesters based on ambient structural vibrations. As a result, these devices are inherently limited to relatively low power outputs. Table 1.1 gives a comparison of currently available vibration energy harvester products.

Company	Dimension (mm^3)	Operating Vibration frequency (Hz)	Output Volt DC	Acceleration amplitude 'g' value	Power output (mW)	Capacitive storage (μF)
AdaptivEnergy Joule thief module	60 x 25 x 25	14	3.6	0.075	0.18	66
ACI -Harvester –III H30	165 x 35 x 40	30	3.0	3	--	100
ACI: Harvester – III H60	125.3 x 50 x 22.5	60	3.0	3	--	100
ACI: Harvester – III H120	125.3 x 50 x 22.5	120	3.0	3	--	100
ACI: Harvester – III H220	110.2 x 56 x 23.5	220	3.0	3	--	100
Mide: Volture PEH25w	92 x 43.8 x 9.9	75-175	N.A.	0.35-1.8	3 – 31 at 50 Hz	0.2
Perpetuum: PMG17 – 100	55 dia, 55 height	100	4.5	0.025 - 1	1 – 45	N.A.

Table 1-1 Comparison of currently available vibration energy harvester products.

There have been limited studies in past on harvesting energy from aerodynamic instabilities [16]. Wang and Ko [17] have carried out studies to harvest energy from flow-induced vibrations. Their base-excited energy harvester converts flow energy obtained from pressure excitation into electricity by oscillation of a piezoelectric sheet. They generate an output power of 0.2μW at an excitation frequency of 26 Hz. Barrero-Gil et al. [18] theoretically investigated the feasibility of energy harvesting from structures undergoing galloping. They represented the sectional aerodynamic characteristics using a cubic polynomial and obtained an expression for the harnessable energy. Specific methods for energy extraction were not discussed. Robbins et al. [19] investigated the use of

flexible, flag-like, piezoelectric sheets to generate power while flapping in an incident wind.

Energy harvesting from flutter phenomenon has also become known. Self-excited oscillations or flapping of a tensioned membrane incident to wind flow can be referred to as flutter. Humdinger wind energy [20] is a recently formed company that researches and develops windbelt generator. Windbelt is a harvesting device that uses a tensioned membrane undergoing a flutter oscillation to extract energy from the wind. It uses electromagnets to generate electricity from the flutter of the membrane.
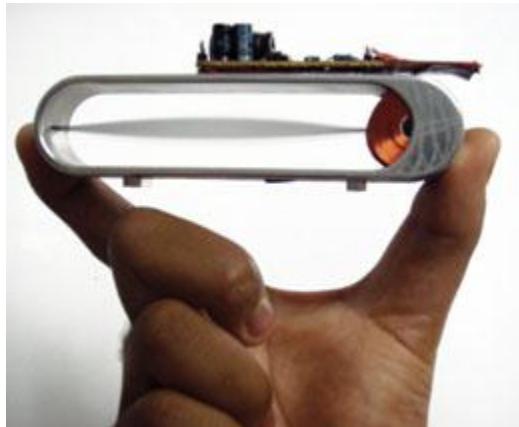
Figure 1-3: Humdinger energy [11] windbelt device

1.3   Applications

The availability of low-power micro-sensors, actuators, and radios is enabling the application of distributed wireless sensing to a wide range of applications such

as smart spaces, medical applications, and precision agriculture [21][22]. Sensor networks can remotely report temperature, moisture and sunlight intensity in farms, to a central computer. Wang et al. [23] have described a wireless sensing prototype system specially designed for structural monitoring of a bridge. Mainwaring et al. [24] have provided an in-depth study of applying wireless sensor networks to real-world habitat and environmental monitoring such as monitoring seabird nesting environment in an ecological reserve. They describe the power requirement for each node to be 6.9mAh per day. The 'eKo system' by Crossbow Technology Inc. [25] is a similar application of outdoor wireless sensing in fields which however, uses a miniature solar panel for powering the sensor network . Evans and Bergman [26] are leading a USDA research group to study precision irrigation control. Wireless sensors were used in the system to assist irrigation scheduling using combined on-site weather data, remotely sensed data and grower preferences. Table 1.2 gives a summary of wireless sensor technology manufacturers and their respective applications.

Company	Sensor Technologies	Sensor Application
Crossbow	Motes: Mica2, Mica2Dot, MicaZ Gateway nodes: Stargate,MIB600 Interface board: MIB600 Ethernet, MIB510 Serial, MIB520 USB	Seismic structural monitoring, indoor/outdoor environmental monitoring, security protection and surveillance monitoring, inventory monitoring, health monitoring
Sentilla (Moteiv)	Motes: T-mote sky Gateway nodes:T-mote Connect	Indoor and outdoor monitoring applications
Dust Networks	SmartMesh-XT motes: M1030, M2030, M2135 SmartMesh-XT manager: PM1230, PM2030, PM2130	Building automation monitoring, industrial process monitoring, and security and defense monitoring
Millenial net	MeshScape 916 MHz and 2.4 MHz: mesh node, mesh gate, end nodes Mesh485: mesh sub-based router, mesh router, and mesh bridges	Building monitoring and industrial process monitoring
Sensicast	Sensicast EMS and RTD nodes Sensicast gateway bridge, mesh Router	Industrial monitoring of temperature and energy

Table 1.2: Summary of wireless sensor technology applications [27]

Most of the wireless sensor network systems are powered by batteries. Replacement of depleted batteries for large network systems is expensive, often impractical and environmentally unfriendly. Hence, the use of energy harvesting methods to power the sensors on-site can be beneficial. Energy harvesting reduces dependency on battery power. The harvested energy may be sufficient to eliminate battery completely. It reduces maintenance costs and eliminates battery replacement labour. This is especially important in outdoor locations such as

inaccessible terrain, geological parks where human interaction is minimum. Powering the wireless sensors, located outdoors, by means of wind energy is a practical alternative to battery power sources.

A piezoelectric energy harvesting device based on a galloping cantilever beam is described in the present work. Such a device has the primary advantages of simplicity and robustness, and could be collocated with the wireless sensors to provide a source of renewable wind energy.

2. Theory of Galloping

Galloping theory for D-section and triangular section is discussed in the following sub sections. The motivation for performing research in this area came from a simple galloping experiment. The apparatus is shown in Fig 2-1. A semi circular wooden bar (12 inch long and 1 inch in diameter) is suspended by four springs. The natural frequency is kept low (<10 cycles per second). When the apparatus is placed in front of an axial fan, the bar builds up vibrations. Energy is being added into the system and the bar can sustain its oscillations over time, inspite of structural damping of the system. Galloping is dependent on the shape and size of the body subjected to transverse air flow. In the following sections, the theory of galloping for two geometrical cross sections has been discussed in detail.
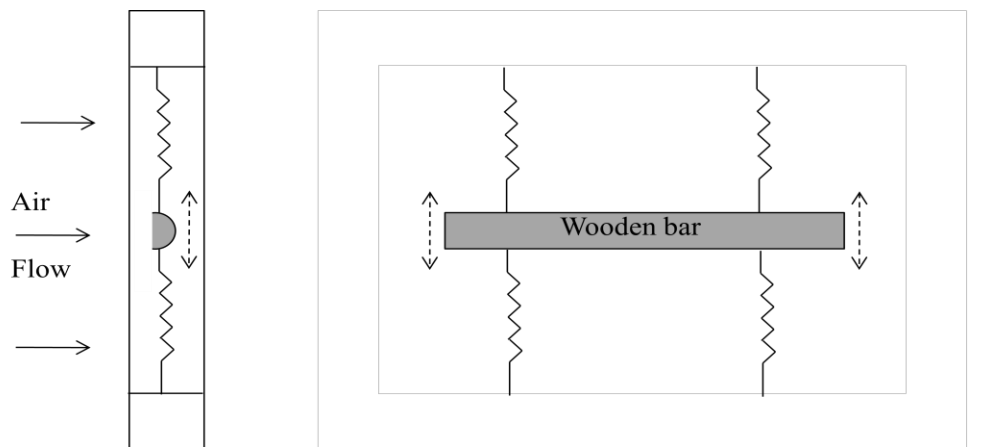
Figure 2-1: Schematic of a galloping beam experiment in lab

2.1 'D – Section'

Consider a prismatic structure with a D-shaped cross-section mounted on a flexible support, exposed to incident wind with a velocity V∞ along the x-direction as shown in Figure 2-1. . Initial perturbations generated by the vortices shed from the D-section result in small, periodic oscillations normal to the direction of incident wind. Let the section be moving downward with a velocity $\dot{y}$ (defined as positive in the positive y-direction). The instantaneous angle of attack α is given by:

$$\alpha = \tan^{-1}\frac{V_a}{V_\infty} \;=\; -\; \tan^{-1}\frac{\dot{y}}{V_\infty} \tag{1}$$

where 'V_a' is the apparent velocity of the air, equal in magnitude and opposite in direction to $\dot{y}$. Va is defined as positive in +y direction. α depends upon the velocity $\dot{y}$ of the galloping body and on the free air flow velocity.
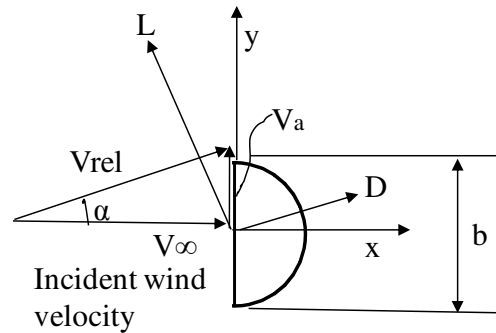
Figure 2-1: Forces on a D-section in an incident wind

16

It is seen that α depends upon the velocity $\dot{y}$ of the galloping body as well as on the incident velocity. The quasi-steady lift force L and drag force D (per unit length) on the section are given by:

$$L = \frac{1}{2} \rho \, V_\infty^2 . b. C_l(\alpha) \tag{2}$$

$$D = \frac{1}{2} \rho \, V_\infty^2 . b. C_d(\alpha) \tag{3}$$

where b is the characteristic length normal to incident flow (chord of the D-section), ρ is the air density, and C_l, C_d are the sectional lift and drag coefficients respectively. Previous research has shown that it is sufficient to include only quasi-steady aerodynamic forces in the analysis, because the characteristic time scale of the system (b/V_∞) is much smaller than the galloping time period [18] .

The components of the lift and drag along the y-direction give the instantaneous excitation force per unit length F_y as:

$$F_y(\alpha) = D \sin\alpha + L \cos\alpha = \frac{1}{2} \rho \, V_\infty^2 . b. C_{F_y}(\alpha) \tag{4}$$

where the coefficient of the force in the y-direction, C_{Fy}, is given by:

$$C_{F_y}(\alpha) = [C_l + C_d \tan\alpha] \cos\alpha \tag{5}$$

Typical 2D (two-dimensional) sectional lift and drag coefficients for a D-section were measured by Ratkowski [28], and are shown in Fig. 2-2. Note that the angle of attack (plotted along the x-axis) is defined as the angle between the incident wind and the flat face of the D-section. For a D-section oriented as shown in Figure 1, the angle of attack is close to 90°. In this region, it is seen that

17

the lift coefficient C_l is approximately linear and has a negative slope. The drag coefficient C_d is approximately constant.
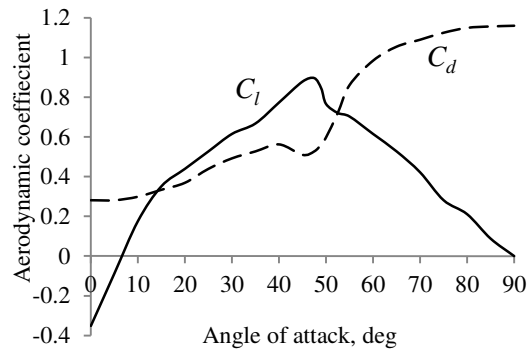
Figure 1-2: C_l and C_d plots for a D-section, from Ratkowski [27]. The angle of attack is defined with respect to the flat face.

Let the flexible support structure have an effective mass per unit length of 'm', damping factor 'ξ' and stiffness '$m\omega_n^2$'. The equation of motion of the D-section mounted on the flexible support is basically that of a linear spring mass damper oscillator with a forcing term 'F_y' that is a function of angle of attack α, and therefore depends on the velocity of the D-section. The equation of motion is given by:

$$m[\ddot{y} + 2\xi\omega_n\dot{y} + \omega_n^2 y] = F_y(\alpha) \tag{6}$$

For small displacements from the equilibrium position (α=0),

18

$$F_y = \frac{\partial F_y}{\partial \alpha} \alpha = \frac{1}{2} \rho\, V_\infty^{\,2} \cdot b \cdot \frac{\partial C_{Fy}}{\partial \alpha} \tag{7}$$

where the dependence of the force coefficient C_{Fy} with angle of attack is given by:

$$\frac{\partial C_{Fy}}{\partial \alpha} = \left(\frac{dC_l}{d\alpha} + C_d \right) \tag{8}$$

Hence, for small α, Eq.(6) can be written as:

$$m[\ddot{y} + 2\xi\omega_n \dot{y} + \omega_n^{\,2} y] = -\frac{1}{2} \rho\, V_\infty^{\,2}\, b \left(\frac{dC_l}{d\alpha} + C_d \right) \frac{\dot{y}}{V_\infty} \tag{9}$$

Equation (9) represents the general equation of motion governing galloping of the structure. It is seen that the forcing term acts as an additional damping due to its dependence on $\dot{y}$. Unstable oscillations, i.e., galloping, occur when the effective damping of the system becomes negative. For low values of ξ, the condition for galloping to occur can be written as:

$$\left(\frac{dC_l}{d\alpha} + C_d \right) < 0 \tag{10}$$

Equation (10) is known as the Den Hartog criterion 0 and can be used to estimate when galloping will occur on any given structure. This criterion depends only on the sectional aerodynamic coefficients; specifically, galloping occurs when

$$\frac{dC_l}{d\alpha} < - C_d \tag{11}$$

From Figure 2-2, it is seen that this condition is satisfied for the D-section when the incident wind is perpendicular to the flat face. The negative damping

factor 'ξ' during galloping condition indicates that energy is extracted by the structure from the air stream. This energy can be harvested and used as a power source.

2.2 Triangular Section

Similar to a D-section, a triangular section also undergoes galloping oscillation when subjected to wind. Alonso et al. [29] discuss galloping instability of triangular section bodies in particular. Equations (1) to (11) are valid also for the triangular section arrangement shown in Fig 2-3. For an isosceles triangular section, let α_o be the angle of attack with respect to incident wind velocity, and β be its main vertex angle. β is a key geometrical parameter affecting the sectional aerodynamic characteristics and hence the galloping stability.
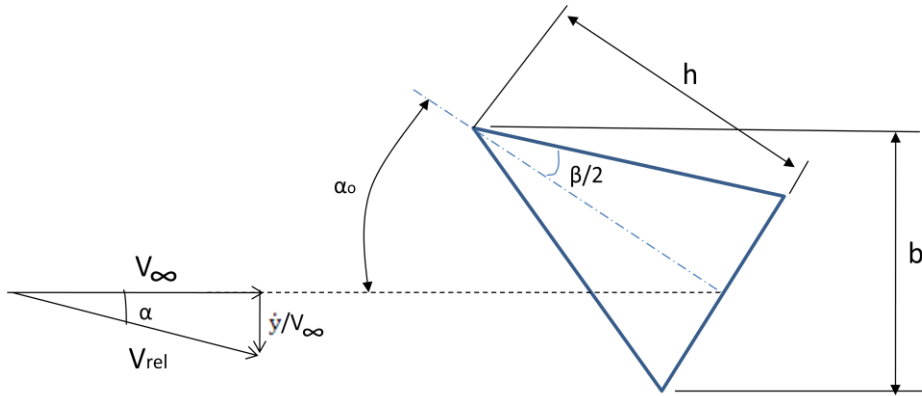
Figure 2-3: Parameters of an isosceles triangular section body subjected to incident wind velocity

The studies conducted by Alonso et al. [29] helped in a second choice of a triangular section to build the galloping device.

20

3. Physical mechanism of the galloping device

Two Galloping devices are investigated to demonstrate energy harvesting capabilities. Galloping device (I) is made of a body having D-section with flat face facing the incoming wind. Galloping device (II) is made of a body having triangular section with flat face facing the incoming wind. These devices are described in the following sections 3.1 and 3.2.

3.1 Device based on D – section
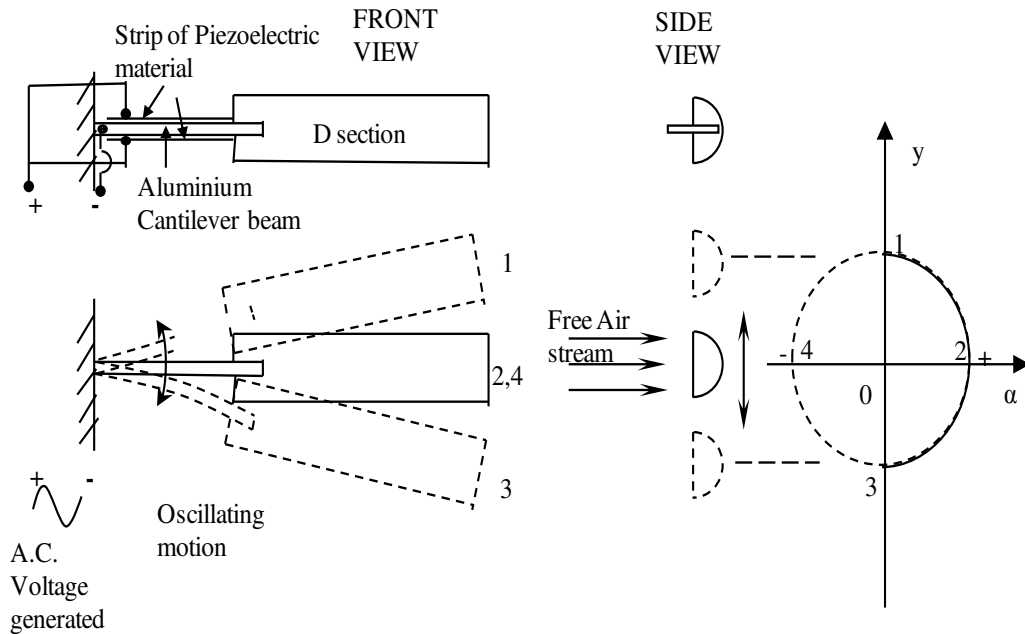
Figure 3-1: Schematic of galloping device (I) showing galloping mechanism and change in instantaneous angle of attack α

21

A galloping device (I) developed as a part of this study consists of a rigid wooden bar 235 mm long, having D-shaped cross section of 30 mm diameter. The bar is attached to the tip of an aluminum cantilever beam. The aluminum beam size (in mm) is 90 x 38 x 0.635. The schematic of the device (I) is shown in Fig. 3-1. The beam is initially held at rest. The direction of incident wind is normal to the flat surface of the D-section, which corresponds to an angle of attack of 90° as defined in Fig 3-1. For angles of attack in this range, the lift curve slope of the D-section is negative, and the Den Hartog criterion is satisfied. As a result, the D-section is prone to galloping. Initial perturbations are caused by vortex shedding and the D-section begins to gallop in a direction transverse to the plane of the beam. The resulting oscillatory bending displacement of the beam progressively increases in magnitude as energy is transferred from the incident wind to the structure. Piezoelectric sheet elements (PZT) bonded to the top and bottom surface of the aluminum beam generate an alternating voltage in response to the bending induced by the galloping D-section. In a practical wind energy harvester, the generated electrical energy would be stored or used to power other devices, however, in the present study, the voltage is simply discharged across a load resistance.

The load resistance across the piezoelectric sheets dissipates energy in the form of Ohmic heating and hence, acts as an additional positive damping on the system. Therefore the amplitude of oscillation of the beam increases till a steady state is reached, wherein the energy extracted from the incident wind is exactly

22

equal to the energy dissipated across the load resistance. In this steady state, the amplitude of oscillation remains constant. For a given incident wind velocity, the induced angle of attack is a function of the beam tip displacement, oscillation frequency, tip slope and location along the tip body.

3.2   Device based on a triangular section

This section examines the effects of cross-sectional shape and angle of attack on transverse galloping stability of a triangular section. Published data on triangular section are used to determine its geometry and aerodynamic characteristics for maximum energy extraction. Alonso and Meseguer [30] have analyzed the effect of main vertex angle β and angle of attack α on galloping stability of triangular section bodies. Their study identified unstable regions in the (α, β) plane. Figure 3-2 shows these zones. Alonso and and Meseguer [30] tested nine triangular prisms having sharp edges, the main vertex angle ranging from $\beta = 10^{o}$ to 90° in 10 degree increment. Section C_l and C_d data results for these nine prisms were thus obtained through wind tunnel experiments over a range of 0 to 180° angle of attack. The Den-Hartog criterion $(\frac{dC_l}{d\alpha} + C_d < 0)$ is applicable to a triangular section also and it is evaluated in the (α, β) plane. When plotted it results in Fig 3-2. Unstable regions can be identified where the Den-Hartog criterion is negative.

23
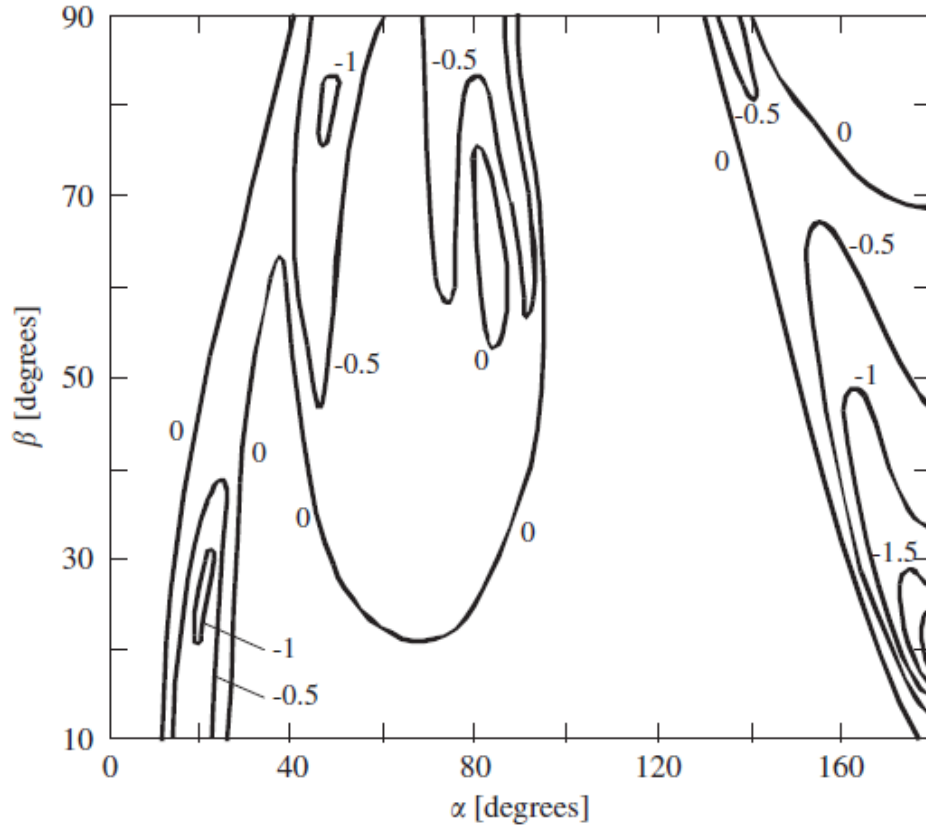
Figure 3-2: Stability diagram in the angle of attack-main vertex angle plane (α, β). Numbers on the curves indicate the value of ($\frac{dC_l}{d\alpha} + C_d$) Note that the stability diagram is symmetric with respect to α = 180° [30]

Galloping of triangular cross-section bodies is more favourable when the base of the triangle is facing the incident wind stream. Figure 3-2 shows how the unstable zones lie around α = 60° and α = 180°. The aerodynamic drag coefficient (C_d in ($\frac{dC_l}{d\alpha} + C_d$)) is larger when there is a separation of flow behind the triangular

24

cross-section. As the main vertex angle β increases, separation of flow increase, and thus the magnitude of drag force also increases. A large angle β is undesirable, since it reduces the value of $(\frac{dC_l}{d\alpha} + C_d)$ term. Although the unstable zone close to α = 180° becomes wider as value of β increases, the value of $(\frac{dC_l}{d\alpha} + C_d)$ term reduces with larger β. For very small angle β, the instability region near α = 60° and α = 180° is narrow. Hence, very small angle β is undesirable. For β < 60°, although $(\frac{dC_l}{d\alpha} + C_d)$ is more negative in value, the unstable range of α near 180° is narrow. Galloping motion depends on angle of attack α and occurs for only a certain range of α. A narrow unstable range of α would be undesirable. On the other hand, for β > 60°, the unstable range of α near 180° is wide, however, $(\frac{dC_l}{d\alpha} + C_d)$ is less negative in value and is close to zero. But a more negative value is desirable to maximise galloping amplitude. Hence, as a trade off, an equilateral triangular section (β = 60°) is selected as the best preferred geometry to produce galloping. Figure 3-3 shows the C_l, C_d plot for equilateral (β = 60°) triangular section. At α = 60°, the base of the triangular section is facing the incoming wind stream, and such an orientation is desirable for galloping to occur. The range of α in these regions for instability is wide. The negative C_l slope region ranges from α = 25° to 95°, where α = 60° being the mean position. The galloping will continue as long as the angle of attack stays within this region.
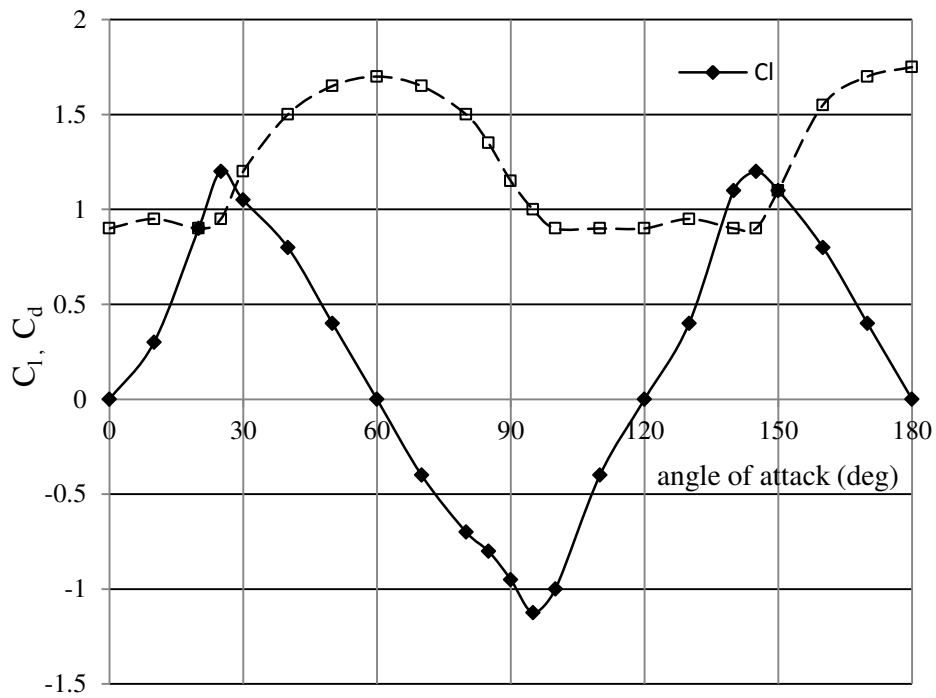
Figure 3-3: C_l, C_d plot for an equilateral triangular section (vertex angle $\beta = 60^o$) [30]

A 2nd galloping device (II) is developed as shown in Fig 3-4, and it consists of a 251 mm long tip body with an equilateral triangular section (each side 50 mm) attached to two elastic beams, 161 mm long each, at both ends. As discussed before, the base of the triangular section faces the incident wind, implying the angle of attack α_o at mean equilibrium position is 60°.

TOP VIEW

$\alpha_o = 60^o$

V_∞

Elastic beam

Elastic beam 1

Triangular tip body

V_∞

SIDE VIEW
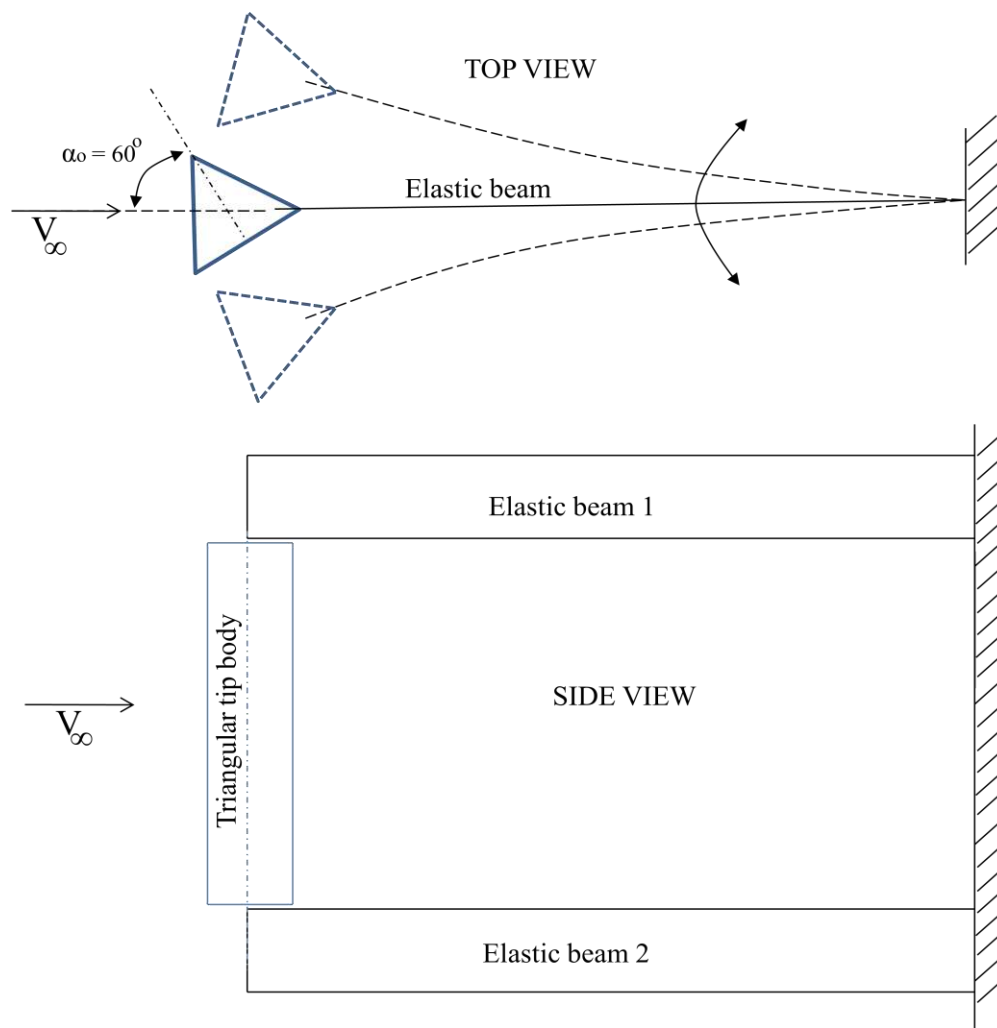
Elastic beam 2

Figure 3-4: Schematic of galloping device (II) with a triangular section tip body attached to an elastic beam, subjected to incident wind speed

4. Analytical Model

A coupled electromechanical model of the galloping energy harvesting device is developed from a mechanics based approach, using the coupled electromechanical energy of the system (see Sodano et al [6] , Lee [31], Nisse [32]) The goal of the model is to predict the voltage generated by the PZT as a function of time, for a given incident wind speed, beam geometry and load resistance. The model consists of two parts: the structural model and the aerodynamic model. Devices with different tip bodies can be modeled using different aerodynamic models in conjunction with the same structural model.

## 4.1 Structural model:

The constitutive equations of a piezoelectric material, relating the strain ϵ and electric displacement D to the mechanical stress σ, and electric field E are given by **Error! Reference source not found.**:

$$\begin{bmatrix} \epsilon \\ D \end{bmatrix} = \begin{bmatrix} s^E & d \\ d^T & e^\sigma \end{bmatrix} \begin{bmatrix} \sigma \\ E \end{bmatrix} \tag{12}$$

where s^E is the compliance matrix, e^σ is the matrix of dielectric constants, and d is the piezoelectric coupling matrix. The superscripts E and σ signify quantities measured at constant electric field and mechanical stress, respectively.

28

The potential energy U of the device consists of terms due to mechanical strain energy as well as electrical energy, and is given by:

$$U = \frac{1}{2}\int_{V_s} \boldsymbol{\sigma}^T \boldsymbol{\epsilon} \, dV_s + \frac{1}{2}\int_{V_p} \boldsymbol{\sigma}^T \boldsymbol{\epsilon} \, dV_p + \frac{1}{2}\int_{V_p} \boldsymbol{E}^T \boldsymbol{D} \, dV_p \tag{13}$$

where the quantity V_p indicates the volume of the piezoelectric element and V_s is the volume of the base structure. In the case of the device in the present study, Eq.(13) can be simplified by substituting one-dimensional quantities for stress, strain, electric field and electric displacement, yielding:

$$U = \frac{1}{2}\int_{V_s} \sigma_{11}\epsilon_{11} \, dV_s + \frac{1}{2}\int_{V_p} \sigma_{11}\epsilon_{11} \, dV_p + \frac{1}{2}\int_{V_p} E_3 D_3 \, dV_p \tag{14}$$

Because the coupled energy (as opposed to enthalpy) of the system is being considered, it must be expressed in terms of the basic quantities D and ϵ. Dropping the subscripts and substituting for stress and electric field from the piezoelectric constitutive equations gives

$$U = \frac{1}{2}\int_{V_s} Y_s \epsilon^2 \, dV_s + \frac{1}{2}\int_{V_p} Y_p^D \epsilon^2 \, dV_p - \int_{V_p} \frac{k^2}{d(1-k^2)} D\epsilon \, dV_p \tag{15}$$

where the superscripts D and ϵ refer to quantities measured at constant electric displacement and constant strain, respectively. The electromechanical coupling coefficient of the piezoelectric, k is given by:

$$k^2 = k_{31}^2 = \frac{d_{31}^2 Y_p^E}{e^\sigma} \tag{16}$$

Note that

$$Y_p^D = Y_p^E(1 - k^2) \tag{17}$$

29

$$e^\epsilon = e^\sigma(1 - k^2) \tag{18}$$

Using the Euler-Bernoulli theory for a beam in bending yields the strain at any height y from the neutral axis as:

$$\epsilon = -v''y \tag{19}$$

where v'' is the curvature (v is the vertical displacement in the y-direction). The beam displacement v can be assumed as:

$$v(x,t) = \sum_{i=1}^{N} \phi_i(x)r_i(t) = \boldsymbol{\phi r} \tag{20}$$

where $\boldsymbol{\phi}$ is the row vector of shape functions set to satisfy boundary conditions, $\boldsymbol{r}$ is the column vector of temporal coordinates of displacement and N is the number of shape functions included in the analysis. The electric displacement is related to the charge generated q and the area of the electrodes A_p by:

$$D = \frac{q}{A_p} \tag{21}$$

Substituting the above expressions into Eq. 15 yields the potential energy of the device as:

$$U = \frac{1}{2}\int_{V_s} Y_s \boldsymbol{r}^T \boldsymbol{\phi''}^T \boldsymbol{\phi''r} \, y^2 dV_s + \frac{1}{2}\int_{V_p} Y_p^D \boldsymbol{r}^T \boldsymbol{\phi''}^T \boldsymbol{\phi''r} \, y^2 \, dV_p$$

$$+ \int_{V_p} \frac{k^2}{d(1-k^2)} \frac{q}{A_p} \boldsymbol{\phi''r} \, y \, dV_p \tag{22}$$

The kinetic energy T is given by:

$$T = \frac{1}{2}\int_{V_s} \rho_s \dot{v}^2 \, dV_s + \frac{1}{2}\int_{V_p} \rho_p \dot{v}^2 dV_p + \frac{1}{2}m_{tip} \, \dot{v}^2(L) + \frac{1}{2}I_{tip}(\dot{v}(L))^2 \tag{23}$$

The quantities m_{tip} and I_{tip} correspond to the mass and moment of inertia of the tip body, respectively. Substituting for the assumed displacements, we get

$T =$

$$\frac{1}{2}\int_{V_s} \rho_s \dot{r}^T \phi^T \phi \dot{r} dV_s + \frac{1}{2}\int_{V_p} \rho_p \dot{r}^T \phi^T \phi \dot{r} dV_p + \frac{1}{2}m_{tip} \dot{r}^T \phi(L)^T \phi(L)\dot{r} + \frac{1}{2}I_{tip}\dot{r}^T \phi'(L)^T \phi'(L) \dot{r}$$

$$(24)$$

The external virtual work done on the system is given by:

$$\delta W = \delta v(L)F_{tip} + \delta v'(L)M_{tip} - \delta q.\mathbb{V} \tag{25}$$

where F_{tip} and M_{tip} are the external forces and moments acting at the tip of the beam, and $\mathbb{V}$ is the voltage across the electrodes on the piezoelectric sheets. The governing equations of the system can be derived from the potential energy, kinetic energy and virtual work either by using Hamilton's principle or by applying Lagrange's equations. The governing equations are:

$$\boldsymbol{M}\ddot{r} + \boldsymbol{K}r + \boldsymbol{\Theta}^{\mathrm{T}}q = F_{tip}\phi_{tip} + M_{tip}\phi'_{tip} \tag{26}$$

$$\boldsymbol{\Theta}r + \frac{q}{C_p} = -\mathbb{V} \tag{27}$$

In the above equations, the effective mass matrix $\boldsymbol{M}$ is given by:

$$\boldsymbol{M} = \int_{V_s} \rho_s \phi^T \phi \, dV_s + \int_{V_p} \rho_p \phi^T \phi \, dV + m_{tip} \, \phi(L)^T \phi(L) + I_{tip}\phi'(L)^T \phi'(L) \tag{28}$$

The effective stiffness matrix $\boldsymbol{K}$ is given by:

$$\boldsymbol{K} = \int_{V_s} Y_s {\phi''}^T \phi'' y^2 dV_s + \int_{V_p} Y_p^D {\phi''}^T \phi'' y^2 \, dV_p \tag{29}$$

A coupling vector $\boldsymbol{\Theta}$ can be defined as:

$$\boldsymbol{\Theta} = \int_{V_p} \frac{k^2}{dA_p(1-k^2)} \phi'' \, y \, dV_p \tag{30}$$

The capacitance of the piezoelectric sheets, C_p is given by (assuming a uniform cross-section and a piezoelectric sheet of thickness t_p):

$$C_p = \frac{e^\epsilon A_p}{t_p} \tag{31}$$

In addition, for the present system, the voltage and charge are coupled together by the load resistance R_L connected across the electrodes of the piezoelectric sheets. This relation can be expressed as:

$$\mathbb{V} = iR_L = \dot{q}R_L \tag{32}$$

Eq.(26) and Eq.(27), in conjunction with the voltage-charge relation given by Eq.(32) represent a coupled electromechanical model of the power harvesting device. To account for structural damping, an additonal proportional damping matrix $\boldsymbol{C}$ is incorporated.

$$\boldsymbol{C} = \alpha \boldsymbol{M} + \beta \boldsymbol{K} \tag{33}$$

where α and β are determined from:

$$\zeta_i = \frac{\alpha}{2\omega_i} + \frac{\beta\omega_i}{2} \qquad i = 1,2,..N \tag{34}$$

In the above equation, ω_i is the natural frequency of the ith mode, ζ_i is the modal damping, and N is the number of modes (equal to the dimension of the mass and stiffness matrices). These quantities are measured experimentally from the impulse response of the beam with an appropriate electrical boundary condition for the piezoelectric sheets.

4.2   Aerodynamic model:

The aerodynamic model will vary for D-section and triangular section. The right hand side of Eq.(26) represents the forcing function.

4.2.1   Galloping device (I) based on D-section
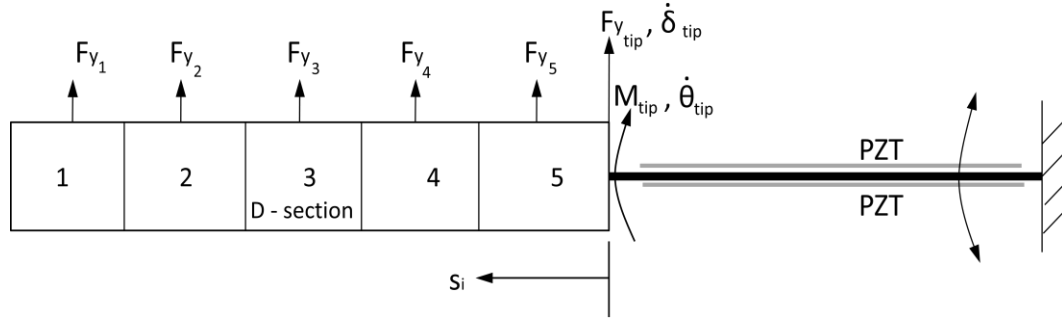
Figure 4-1: Schematic of device (I) showing spatial discretization over tip body of D-section

The tip of the beam is subjected to aerodynamic force F_{tip} and tip moment M_{tip} that are due to the sectional aerodynamic force F_y integrated over the length L of the tip body.

$$F_{tip} = \int_0^L F_y \, ds = \int_0^L [L \cos(\alpha) + D \sin(\alpha)] \, ds \tag{35}$$

$$M_{tip} = \int_0^L F_y \cdot s \, ds \tag{36}$$

where s is the length coordinate along the tip body. Due to the geometry of the device, the sectional angle of attack is a function of rate of change of beam tip displacement, rate of change of beam tip slope and the location of the section along the tip body. The section angle of attack accounts for the rotation of the tip body. It is given as:

33

$$\alpha(s) = -\frac{s\dot{y}'(L) + \dot{y}(L)}{V_\infty} \tag{37}$$

The sectional lift and drag coefficients were obtained from the data measured by Ratkowski [28] (Fig. 2-2). Note that the angle of attack α_{eff} required to use this data is related to the angle of attack in Eq.(37) by:

$$\alpha_{eff}(s) = \frac{\pi}{2} + \alpha(s) \tag{38}$$

4.2.2 Galloping device (II) based on equilateral triangular section

The geometry of the galloping device (II) [Fig. 3-6] is such that, every cross section along the length of the triangular tip body is subjected to the same angle of attack at any given point of time. It implies that the lift force acting at any cross section of the tip body is same over the entire length of the tip body at any instant of time. Hence, it is not required to consider for the rotation effect over the length of the triangular tip body. The calculation of tip aerodynamic force is as follows:

$$F_{y\,tip}\,(triangular) = \int_0^L F_y\,ds = \int_0^L [L\cos(\alpha) + D\sin(\alpha)]\,ds \tag{39}$$

Where F_y is the aerodynamic force per unit length of tip body with triangular section. The tip aerodynamic force is used as external forcing to determine the output of the system. There is no moment acting on the tip body.

The sectional lift and drag coefficients were obtained from the data measured by Alonso [30] (Fig.3-4). Note that the angle of attack α_{eff} required to use this data is related to the angle of attack in Eq.(39) by:

$$\alpha_{eff}(s) = \frac{\pi}{3} - \frac{\dot{y}}{V_\infty} \tag{40}$$
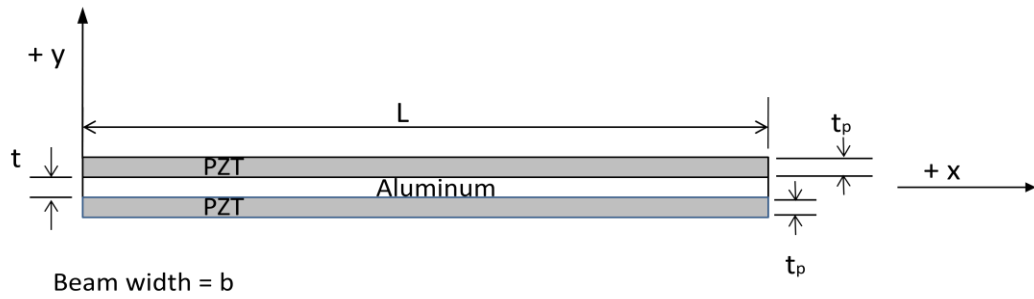
4.3 Solution procedure:

Figure 4-2: Schematic of beam geometry

The constitutive equations of the model [Eq.(26, 27)] were solved by time marching using MATLAB Simulink [34]. A single, cubic shape function is assumed to represent the beam deflection as:

$$v(x,t) = \phi(x)\, r(t) = \left(\frac{x}{L}\right)^3 r \tag{41}$$

where L is the length of the beam. The tip body is discretized into several elements to evaluate the tip force and tip moment as given by Eqs.(33, 34). The schematic of beam geometry with piezoelectric (PZT) sheets is shown in Fig. 4-2.

The block diagram shown in Figure 4-3 describes the solution procedure. The model predicts beam tip response $v(L,t)$, voltage $\mathbb{V}(t)$ generated and current

35

flowing through the load resistance for given values of incident wind velocity, load resistance and device geometry. Tip bodies of any cross-sectional geometry can be evaluated by incorporating the appropriate sectional airfoil characteristics in the form of a table lookup.
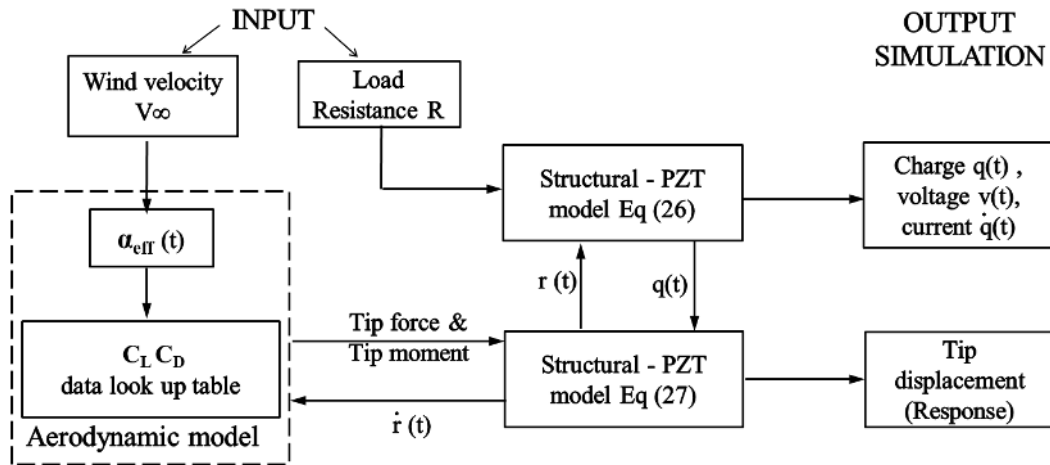

Figure 4-3: **Block diagram of solution procedure in MATLAB Simulink**

5.   Experimental Set up for model verification

5.1   Galloping device (I): D – Section

A prototype galloping beam device was constructed and tested to validate the analytical model. The tip body is a rigid wooden bar 235 mm long, with a D-shaped cross section of 30 mm diameter. The bar is attached to the tip of a 90 mm long aluminum cantilever beam, of width 38 mm and thickness 0.635 mm (see Fig 5-1). Two piezoelectric sheets (PSI-5H4E from Piezo systems, Inc. [35]). of length 72.4 mm, width 36.2 mm and thickness 0.267 mm are bonded to the top and bottom surface of the aluminum beam. The piezoelectric sheets are connected in parallel with opposite polarity, because the top layer undergoes tension when the bottom layer is undergoing compression. In this way, the charges developed by the piezoelectric sheets are added together and the effective capacitance is the sum of the capacitances of the individual sheets. The properties of the beam, tip body and piezoelectric sheets are listed in Table 5-1.

A range of load resistances are connected across the piezoelectric sheets to measure the voltage generated. A NI 9205 data acquisition system in conjunction with Labview was used to acquire the data. A voltage divider buffer circuit was used to scale the generated voltage down to the range of the data acquisition system. The beam was exposed to different wind velocities by placing it in front

37

of a variable speed axial fan. The wind velocity was measured by a digital anemometer. The tip of the beam was initially held at rest. The generated voltage caused by galloping of the beam was measured over a range of incident wind velocities for a constant load resistance. The power generated was calculated based on the generated voltage and the load resistance. The generated voltage was measured over a range of load resistances at a constant wind velocity.
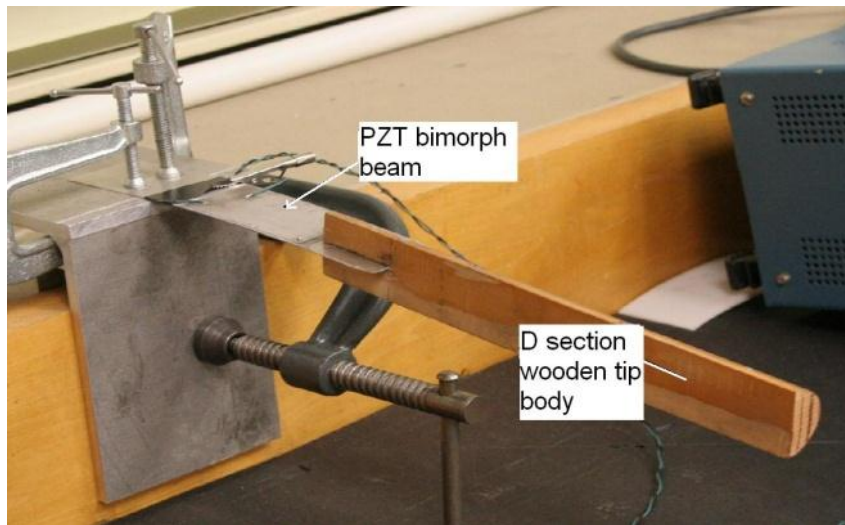

Figure 5-1: Experimental set up showing bimorph beam and attached wooden bar of D section

Property	Symbol	Value
PZT Strain Coefficient (pC/N)	d_{31}	-320
PZT Young's Modulus (GPa)	Y_p^E	62
PZT Dielectric Constant (nF/m)	e^σ	33.64
PZT Density (kg/m^3)	ρ_p	7800
Aluminum Young's Modulus (GPa)	Y_s	70
Aluminum Density (kg/m^3)	ρ_s	2700
Tip Mass (g)	m_{tip}	65

Table 5-1: Properties of Galloping device (I) having tip body with D-section

5.2 Galloping device (II): Triangular section

A galloping device (II) with an equilateral triangular section tip body is built to carry out experiments. The objective is to see the workability of the device. It is decided to verify only the dynamic response obtained through the model. There are no piezoelectric sheets attached to the beam in this device. Styrofoam is used as a convenient material to fabricate the tip body. Each face of the triangular tip body is fabricated on the Roland CNC mill and then bonded together. The edges of the tip body are smoothed using sand paper to achieve a perfect triangle section. The objective of the experiment is to determine the tip displacement of the galloping beam possible for various ranging wind speeds. A dual-axis Analog Devices ADXL322 accelerometer (having range from 2g to -2g) was used for measurement purpose. The accelerometer was mounted at the tip of the beam to

measure acceleration in X and Y direction in the plane of oscillation of the beam. The accelerometer signal is integrated over time to obtain displacement in X and Y direction.
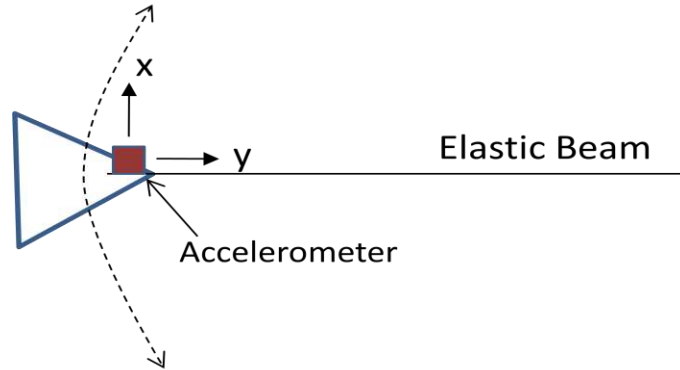

Fig 5-2: Schematic of the accelerometer position on the tip of the beam to measure acceleration in X and Y direction

When the beam is oscillating, its tip moves on a curved path as shown in Fig 5-2. The direction of accelerometer is constantly changing at every time instant. The x displacement measured is the curved path of the tip. x can be assumed to be a straight line since x >> y. The displacement measured in X and Y direction can be shown as follows:

Figure 5-3: Schematic of beam tip displacement

The tip deflection is measured as follows:

$$\delta_{tip} = \sqrt{x^2 - y^2} \tag{42}$$

Where x and y are displacement of beam tip in X and Y direction respectively

The galloping device with two elastic beams, and a triangular section tip body, as shown in Fig 5-4, is mounted in a subsonic wind tunnel at the University of Texas at Austin. The device is mounted in the center of the open section of the tunnel to avoid any tunnel-wall drag and to have a smooth airflow around its body. Constant wind speed is incident on the device. As the flat surface of the triangular tip body faces the incoming wind, the device starts galloping. Signal measurements from the accelerometer are performed using NI data acquisition system for analog signals.
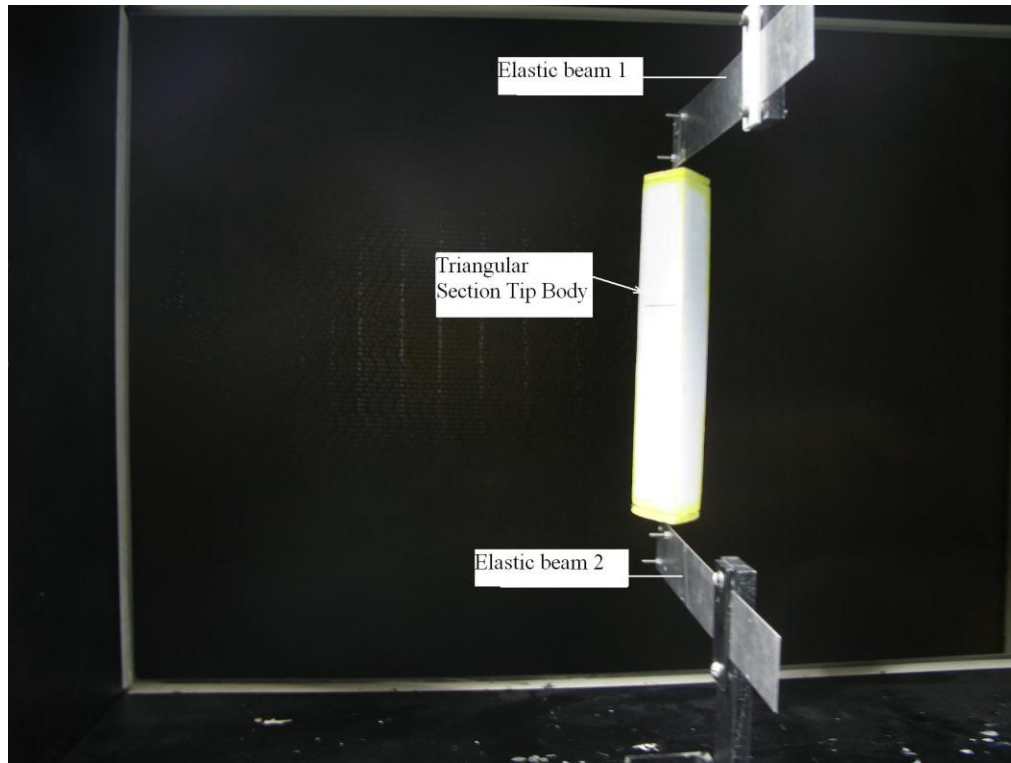
Figure 5-4: Experimental set up showing two elastic beams attached to a triangular section tip body. Location: Subsonic wind tunnel at the University of Texas at Austin
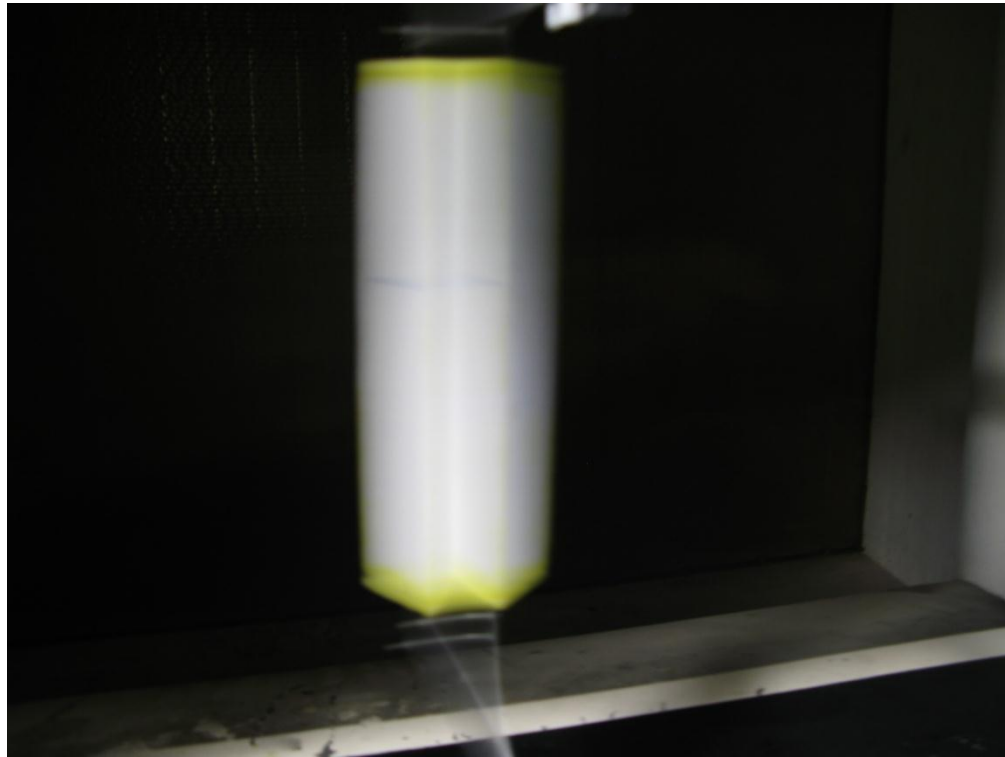
Figure 5-5: A photograph capturing the oscillations due to galloping instability of a tip body with equilateral triangular section attached to elastic beams. Location: Subsonic wind tunnel at the University of Texas at Austin

Table 5-2: Accelerometer Specifications:

Parameter	Conditions	Typical	value	Unit
Measurement range	Each axis		±2	g
Sensitivity at Xout, Yout	$V_s = 3V$		420	mV/g
0 g voltage at Xout, Yout	$V_s = 3V$		1.5	V
Power supply:				
Operating voltage range			2.4-6	V
Supply Current			0.45	mA

Table 5-3: Properties of Galloping device (II) having tip body with equilateral triangular section

Parameter	Symbol	Value	Unit
Beam Density	ρ	2700	kg/m^3
Beam modulus (each)	E	70	GPa
Beam length (each)	L_1, L_2	0.161, 0.112	m
Beam width (each)	b	0.04	m
Beam thickness (each)	t	0.635	mm
Area Moment of inertia (each)	I	0.874	mm^4
Triangular tip body mass	m_{tip}	47.6	g

* Since there are two identical beams attached to the triangular section tip body, all the above parameters related to the beam, refer to each beam.

L_1, L_2 in Table 5-3 refer to two different set of beams used for the galloping device, keeping all other parameters constant. The experiments were conducted for beams of two different lengths, thereby of two different stiffnesses or natural frequencies. The natural frequency for beam of length L_1 is 6.5 Hz and for the beam of length L_2 is 11.2 Hz. Tip mass is kept constant.

$$\text{Beam stiffness, } k = \frac{3EI}{L^3} \tag{43}$$

$$\omega_n = \sqrt{\frac{k}{m_{tip} + 0.23m}} \quad \text{where m = mass of the beam = } \rho.\text{(volume of beam)} \tag{44}$$

6. Results and Discussion

6.1 Galloping device (I): D – Section

The focus of the experiments was to measure the bending response of the beam and the voltage generated by the piezoelectric sheets. These data were used to validate the analysis. The influence of various parameters of the system on the power generated was also studied. Figure 6-1 shows the general trend of measured voltage generated by the piezoelectric sheets starting from rest at a constant incident wind speed. A steady state voltage amplitude of 32V was measured across a 0.7 MΩ load resistance, at a wind speed of 9.5 mph.
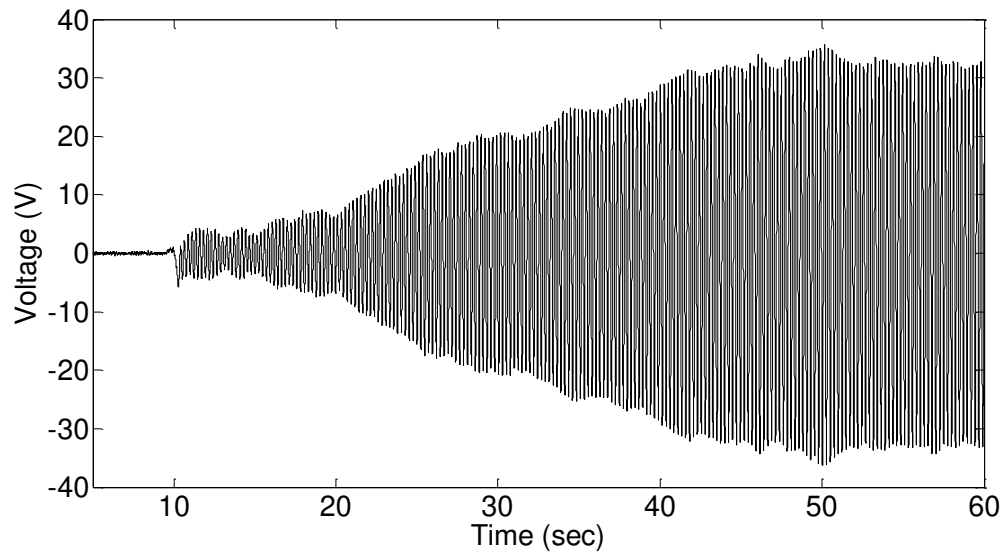

Figure 6-1: Measured voltage generated by the piezoelectric sheets, 0.7MΩ load resistance at wind velocity of 9.5 mph

45

A closer look at the steady state voltage is shown in Fig.6-2. It was observed that the response is predominantly a single mode. The frequency of oscillation was found to be constant irrespective of load resistance or wind velocity, and was equal to the natural frequency (4.167 Hz) of the cantilever beam.
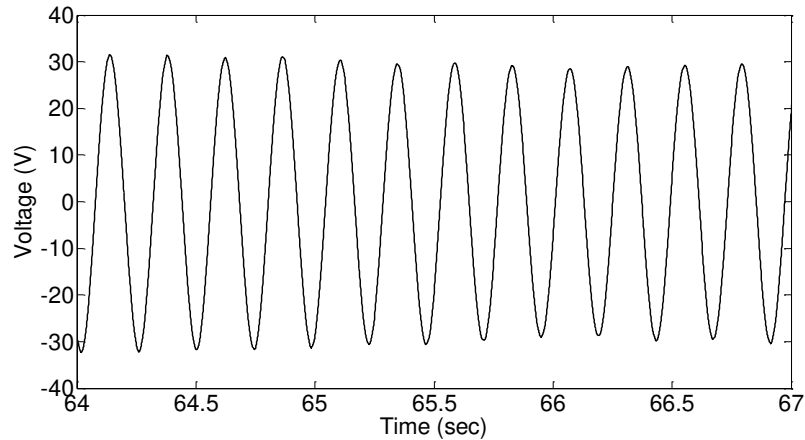

Figure 6-2: Measured voltage generated by the piezoelectric sheets at steady state, 0.7MΩ load resistance at wind velocity of 9.5 mph

The mechanical damping ratio ζ of the cantilever beam is calculated from the impulse response of the beam. The voltage generated by the piezoelectric sheets, with open-circuited electrodes, in response to a tip impulse is shown in Fig.6-3. From these data, the damping is calculated using the logarithmic decrement.
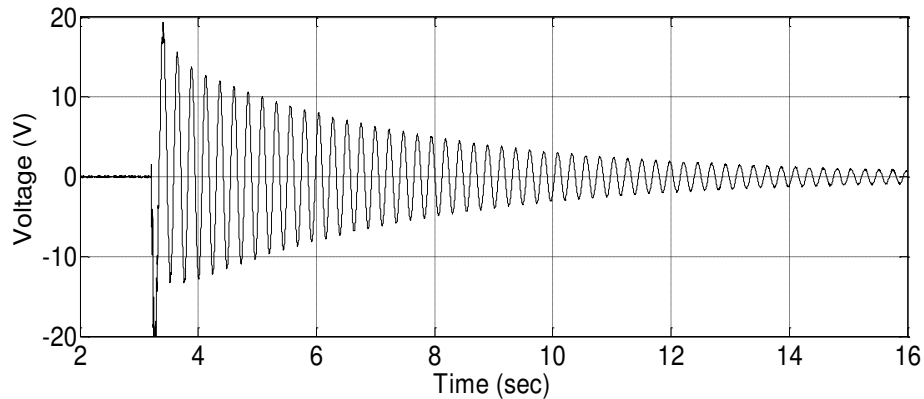
Figure 6-3: Measured impulse response of the beam, with electrodes open-circuited.

The measured voltage was compared to that predicted by the analysis for various load resistances and wind velocities. A comparison of the measured and predicted voltages at steady state, for a load resistance of 0.7 MΩ, is shown in Fig. 6-4. Note that an initial perturbation is introduced in the model to initiate galloping (similar to the effect of the Von Karman vortex street observed in practice) by giving the beam a small tip displacement. A good correlation of both amplitude and frequency is observed. Figure 6-5 shows the voltage generated by the piezoelectric sheets during the transient response of the beam, as calculated by the analytical model. It is seen that the amplitude of the generated voltage increases with time and then reaches a constant value, qualitatively following the transient response measured experimentally (Fig.6-1). It can be concluded that the analytical model can capture both the transient and the steady state behavior of the system.
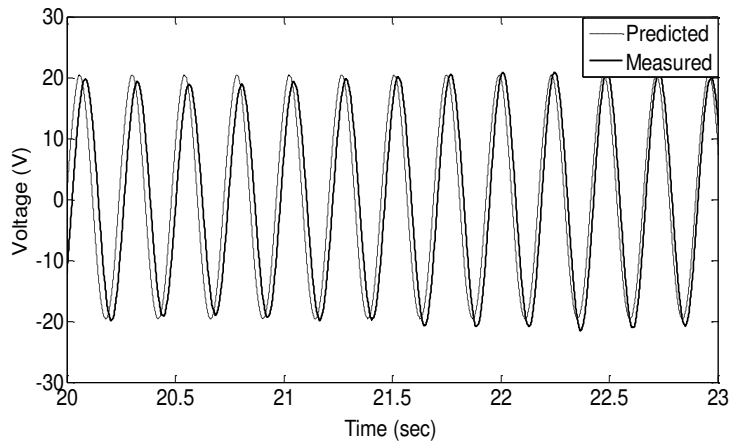
47

Figure 6-4: Comparison of measured and predicted voltage at steady state, 0.7 MΩ load resistance at wind speed of 8 mph.
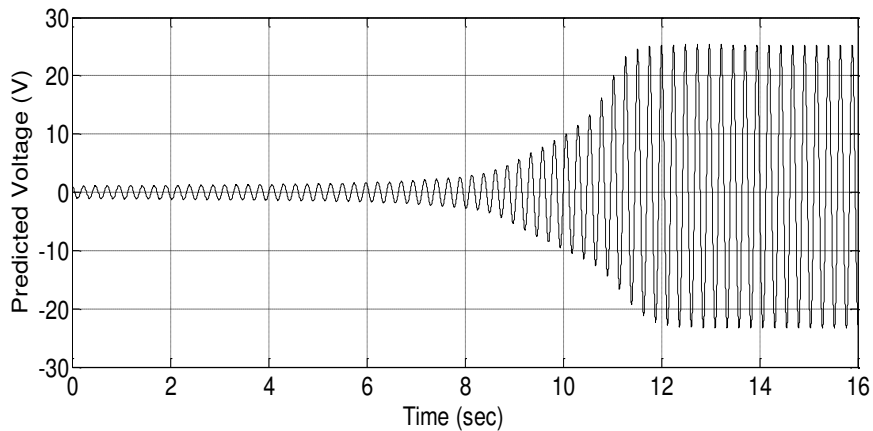
Figure 6-5: Transient response of the beam as predicted by analysis, at incident wind speed of 8.6 mph, and 0.7 MΩ load resistance

Good correlation is also observed between the measured and predicted steady state voltage amplitudes as a function of load resistance (Fig.6-6) and wind speed (Fig.6-7). It is seen that the generated voltage increases approximately linearly with the wind velocity for a given load resistance. Note that the voltage generated

48

by the piezoelectric sheets was on the order of 30V, which implies that small signal electrical characteristics are no longer applicable. This may account for the discrepancies between the predictions and the measured data. Other sources of error could include the effect of the finite thickness bond layer, and discrepancies between the operating conditions (for example, Reynolds number) of the present experimental setup and the experimental setup used for the published aerodynamic coefficients. Although the generated voltage increases with load resistance and wind velocity, the device generates maximum power when the load resistance is optimal. This trend can be seen in Fig.6-8. The power plotted is the average power, which is half of the peak power.

Figure 6-6: Comparison of measured and predicted steady state voltage, as a function of load resistance, at wind speed of 8.5 mph
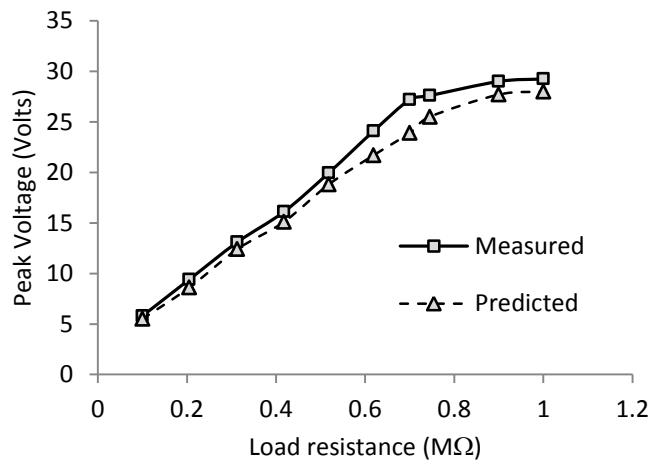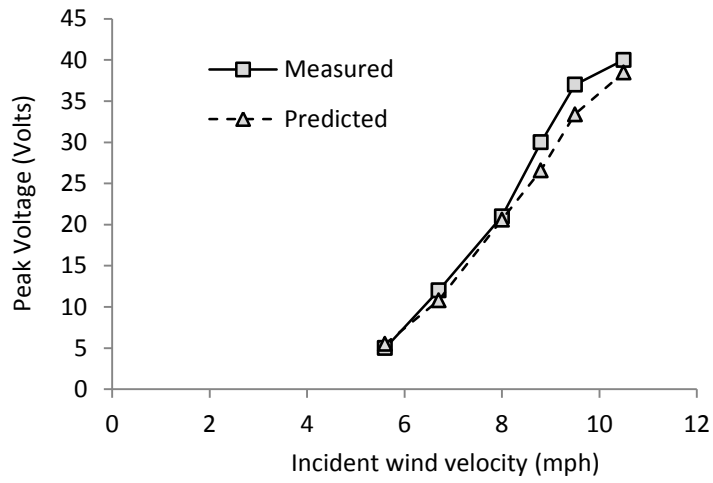
Figure 6-7: Comparison of measured and predicted steady state voltage as a function of

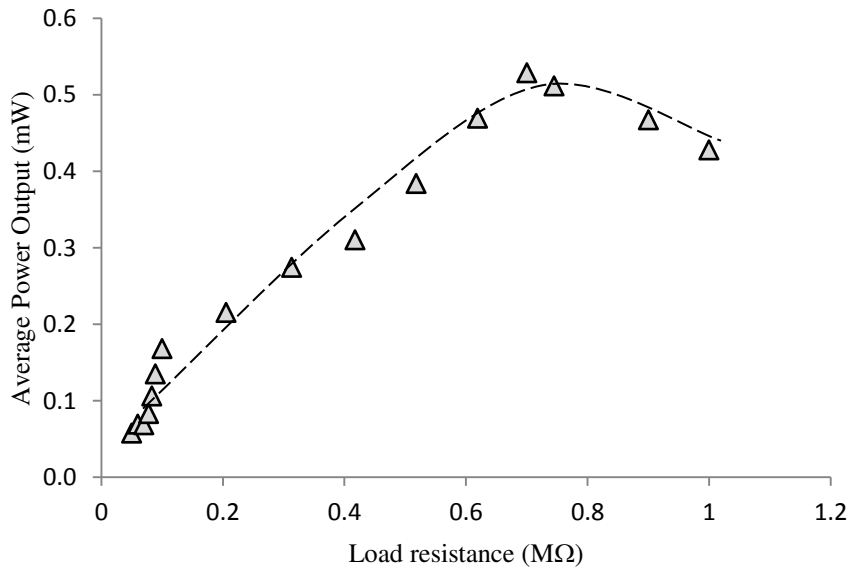**incident wind velocity, for 0.7 MΩ load resistance**

Figure 6-8: Measured power as a function of load resistance, at 8.5 mph wind speed

The variation of measured power output on wind velocity is shown in Figure 6-9, along with analytical predictions. These values correspond to the maximum power output, based on a load resistance of 0.7 MΩ. It is seen that the power output progressively increases with increasing wind velocity. The power output is negligible below a wind velocity of 5.6 mph due to the inherent structural damping in the device. However, annual average wind speed estimates, for example, in region of Texas is around 13 mph [37] , which implies that the range of power output shown Fig.6-9 is practically achievable. For the prototype galloping device, a maximum power output of 1.14mW was achieved at 10.5 mph. Experimental results by Ajitsaria et al. [10] have indicated a maximum power of 250μW produced by their bimorph PZT bender based on harvesting structural vibrations. It can be concluded that it may be possible to harvest larger amounts of power using galloping devices compared to devices based on structural vibrations.
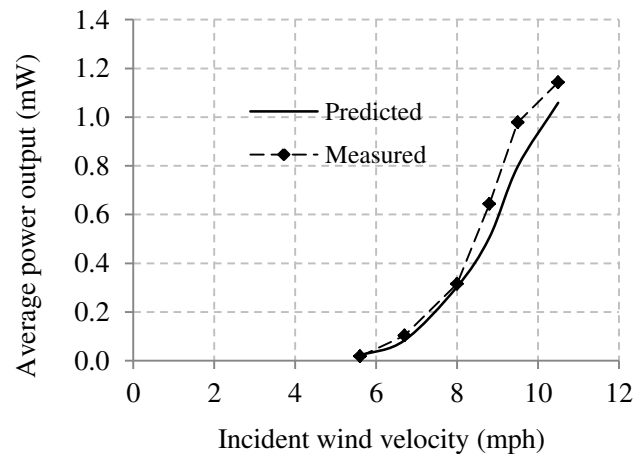

Figure 6-9: Measured and predicted output power versus wind velocity, 0.7 MΩ load resistance.

6.2   Galloping device (II): Triangular Section

An approach similar to D-section is used to measure experimental data for a triangular section galloping device (II). The purpose of these experiments is to verify the dynamic response from the model with measured tip displacement response. Figure 6-10 shows a general accelerometer signal measuring in X and Y direction. The accelerometer is attached to the tip of the beam as shown in Fig. 5-2. Subjected to a constant incident wind speed in the wind tunnel, the signal measured starts from rest, captures the transient response and settles at steady state amplitude. As the angle of attack just goes out of the unstable region of negative C_1 slope, the response attains steady state amplitude. In order to continue extracting energy from the galloping device, it is essential that the galloping operation continues to be within the unstable region. Since there is no piezoelectric material attached to the beam, no energy is being extracted.
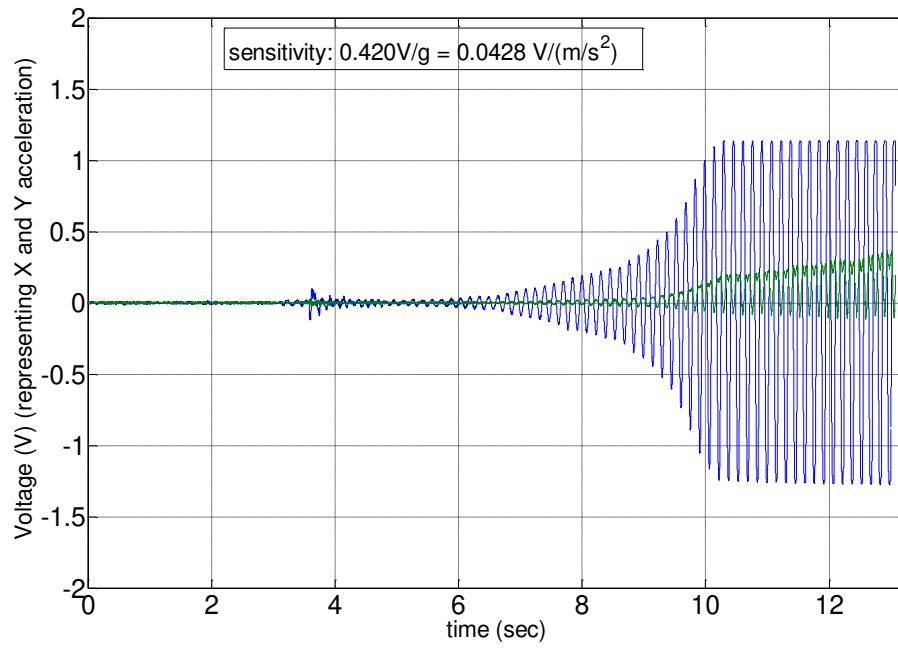
Figure 6-10: Accelerometer voltage signal measuring X (blue line) and Y (green line) acceleration at the tip of the beam, at incident wind speed of 7 mph
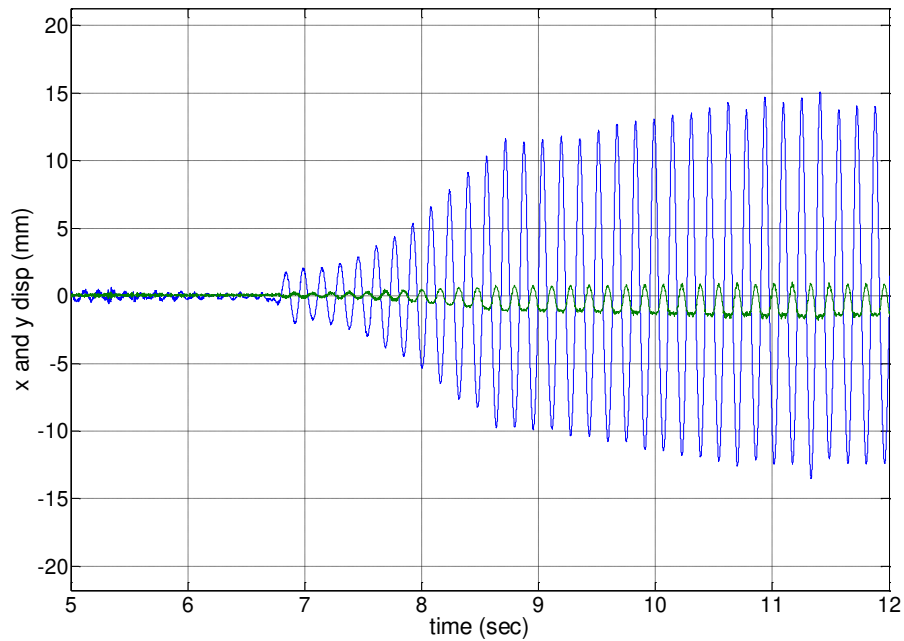
Figure 6-11: Transient tip displacement response (measured) of galloping device (II)

subjected to incident wind speed of 6.4 mph

The accelerometer signal is converted from voltage to acceleration using the sensitivity factor. The acceleration is integrated over time twice to obtain a displacement response of the beam tip. Figure 6-11 shows an integrated signal representing transient response of tip displacement of the galloping beam at 6.4 mph wind speed. Figure 6-12 shows a close look at a steady state measured response at same wind speed. The frequency of oscillation is determined experimentally from the steady state and is found to be 6.5 Hz.

54
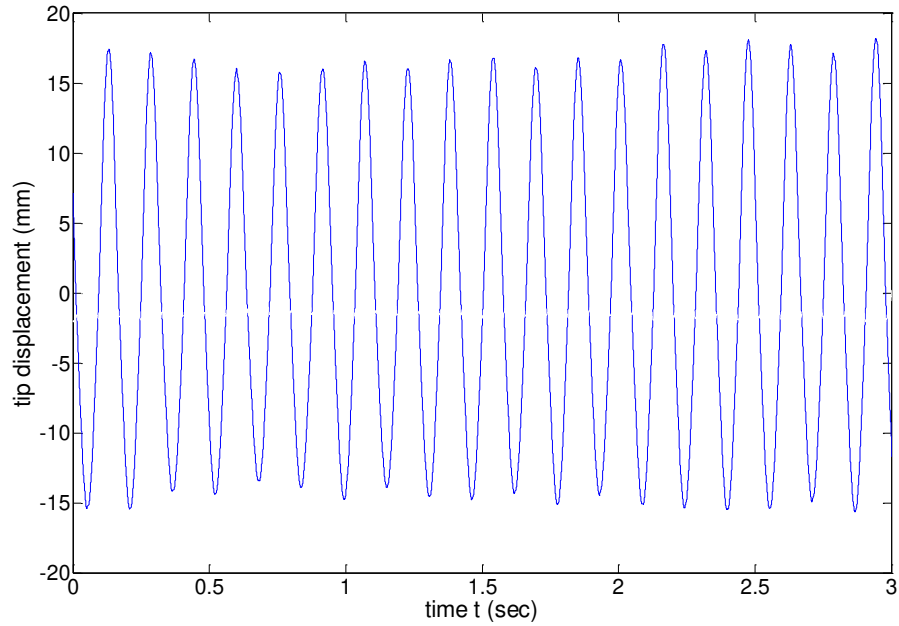
Figure 6-12: Steady state tip displacement response (measured) of galloping device (II)

subjected to incident wind speed of 6.4 mph

Table 6-1: Results for galloping device (II)

|			Measured	Simulated
Wind Speed (mph)	Natural frequency (Hz)	Stiffness of the system (N/mm)	Max. Beam tip deflection (mm)	Max. Beam tip deflection (mm)
6.4	6.5	0.088	31.8	29
7.0	6.5	0.088	32.5	30.5
10.0	11.25	0.260	41	38
11.0	11.25	0.260	43	40.4

The simulated results for steady tip displacement are close to the measured results. They follow a same increasing trend. Increasing wind speed result in an increase in tip deflection, denoting higher strain energy produced in the beam. Measurements are taken for two natural frequencies of the system, by changing

55

the beam length (L_1, L_2: see Table 5-3) and keeping the tip mass constant. In both cases, the beam oscillations are noted to be at the natural frequency, that is, at resonance. To initiate galloping, a higher minimum speed (7.5mph) is required for the system with natural frequency = 11.25 Hz. For the system with lower natural frequency, the corresponding minimum wind speed required is 5 mph. It shows systems with very high natural frequencies may not be suitable for the galloping device.

7. Summary and Conclusion

A device based on galloping piezoelectric cantilever beam was developed to extract power from wind. The beam has a rigid tip body of D-shaped cross section. The tip body undergoes galloping oscillations when subjected to incident wind. Piezoelectric sheets bonded on the beam convert strain energy into electrical energy.

The electrical power generated by a prototype device 325 mm long was measured over a range of wind velocities, and the feasibility of wind energy harvesting using this device was demonstrated. The power output was observed to increase rapidly with increasing wind speed. Due to the structural damping of the beam, a minimum wind velocity of 5.6 mph was required to generate power from this device. For a wind velocity of 10.5 mph, a maximum power output of 1.14mW was measured.

An analytical model was developed including the aerodynamic properties of the tip body, structural properties of the beam and the electro-mechanical coupling of the piezoelectric sheets. Based on incident wind velocity, geometry and other structural parameters of the galloping device, the model could predict the dynamic voltage generated across load resistor, current produced and power output. The model showed good correlation with measured data, and was able to predict both the transient and the steady-state behavior of the device. It was observed that beam geometry and mass parameters, which determine the natural

frequency of the system, play a significant role in the maximum power generated. All these parameters can be optimized within the model to maximise the power output.

Any tip body could be modeled by inputting appropriate sectional aerodynamic data. Based on this data, dynamic angle of attack and aerodynamic forcing on the device was predicted by the model, which in turn predicts power output. In this way, a tip body with optimum aerodynamic properties can be designed to maximize the power output of this device.

A 2nd device based on galloping cantilever beam was developed and tested for workability. The beam of this device has a rigid tip body of equilateral triangular section. A study of the geometry of the tip body was carried out and the equilateral triangle cross-section was observed to be more favourable to cause galloping than other isosceles triangle cross-sections. Aerodynamic data for this geometry was used in the analytical model to predict beam tip response. The predicted result agreed with experimental measurements of beam tip response. Galloping experiment was conducted for two different natural frequencies of the system. Higher natural frequency of the system led to increasing the minimum wind speed required to initiate galloping. This result was in conjunction with the model.

A potential application of power generation using this device is to power wireless sensor devices in large civil structures, exposed to natural wind. It can be concluded that it is possible to harvest significantly more power using this kind of

device compared to a device based on ambient structural vibrations. The device described in this paper forms a baseline for future advancements in development of wind energy based piezoelectric power generators.

8. References

[1]   Den Hartog, J.P., 1956, "Mechanical Vibrations", Dover Publications Inc., New York, pp. 299-305.

[2]   Chabart, O. and Lilien, J. L., 1998, "Galloping of electrical lines in wind tunnel facilities", Journal of Wind Engineering and Industrial Aerodynamics, Vol 74-76, pp. 967-976.

[3]   Alonso, G., Meseguer, J. and Pérez-Grande, I., 2007, "Galloping stability of triangular cross-sectional bodies: A systematic approach," Journal of Wind Engineering and Industrial Aerodynamics 95, pp. 928–940.

[4]   Kazakevich, M. I. and Vasilenko, A. G., 1996, "Closed analytical solution for galloping aeroelastic self-oscillations," Journal of Wind Engineering and Industrial Aerodynamics, 65, pp. 353-360.

[5]   Laneville, A., Gartshore, I. S. and Parkinson, G. V., 1977, "An explanation of some effects of turbulence on bluff bodies" Proceedings of the Fourth International Conference on Wind Effects on Buildings and Structures, Cambridge University Press, pp. 333–341.

[6]   Sodano, H., Park, G. and Inman D., 2004, "Estimation of electric charge output for piezoelectric energy harvesting", Strain, 40 (2), pp. 49-58.

[7]   Umeda M., Nakamura K. and Ueha S., 1996, "Analysis of the transformation of mechanical impact energy to electric energy using piezoelectric vibrator," Japan. J. Appl. Phys. 35, pp. 3267–73.

[8]   Roundy S., Wright P. K. and Rabaey J. M., 2004, "Energy Scavenging for wireless sensor networks with special focus on vibrations," Kluwer Academic Publishers.

[9]   Ottman G. K., Hofmann H. F. and Lesieutre G. A., 2003, "Optimized Piezoelectric Energy Harvesting Circuit Using Step-Down Converter in Discontinuous Conduction Mode," IEEE Trans. Power Electronics, 18(2), pp. 696–703.

[10]   Ajitsaria J., Choe S. Y., Shen D. and Kim D. J., "Modeling and analysis of a bimorph piezoelectric cantilever beam for voltage generation," 2007, Smart Materials and Structures, 16, pp. 447-454.

[11]   Holst Centre, High Tech Campus 31, 5656 AE Eindhoven, Netherlands. <www.holstcentre.com>

[12]   AdaptivEnergy, 1000 Lucas Way Suite B, Hampton VA 23666, USA. <www.adaptivenergy.com>

[13]   Advanced Cerametrics, Inc., P.O. Box 128, 245 N. Main St., Lambertville, NJ 08530, USA. <www.advancedcerametrics.com/pages/energy_harvesting>

[14]   Mide Technology Corporation, 200 Boston Avenue, Suite 1000, Medford, MA 02155, USA. <www.mide.com/products/volture/volture_catalog.php>

[15]   PMG Perpetuum Ltd., Epsilon House, Southampton Science Park, Southampton, SO16 7NS. 5.   www.perpetuum.co.uk

[16]   Jung, H.J., Lee, S.W. and Jang, D.D., 2009, "Feasibility Studies on a New Energy Harvesting Electromagnetic Device Using Aerodynamic Instability", IEEE Transactions on Magnetics, 45(10), pp. 4376-4379.

[17]   Wang D.A. and Ko H.H., 2010, "Piezoelectric energy harvesting from flow-induced vibration", Journal of Micromechanics and Microengineering, 20(2).

[18]   Barrero-Gil A., Alonso G. and Sanz-Andres A., 2010 "Energy harvesting from transverse galloping", Journal of Sound and Vibration, 329(14), pp. 2873-2883.

[19]   Robbins, W. P., Morris, D., Marusic, I. and Novak, T. O., 2006, "Wind-Generated Electrical Energy Using Flexible Piezoelectric Materials", IMECE2006-14050, ASME Publications-AD, Vol. 71, pp. 581—590.

[20]   Humdinger Wind Energy <www.humdingerwind.com>

[21]   Estrin D., Govindan R., and Heidemann J., (Eds.), 2000, "Special Issue on Embedding the Internet. Communications of the ACM", 43(5).

[22]   Badrinath B. R., Srivastava M., Mills K., Scholtz J. and Sollins K., (Eds.), 2000, Special Issue on Smart Spaces and Environments IEEE Personal Communications.

[23]   Wang Y., Kenneth J. Loh, Lynch J. P., Fraser M., Kincho Law and Ahmed Elgamal, 2006, "Vibration Monitoring of the Voigt Bridge using Wired and Wireless Monitoring Systems," The Proceeding of 4th China-Japan-US Symposium on Structural Control and Monitoring'.

[24]   Mainwaring A., Polastre J., Szewczyk R., Culler D. and Anderson, J., 2002, "Wireless sensor networks for habitat monitoring," Proceedings of the 1st ACM international workshop on Wireless sensor networks and applications, Atlanta, Georgia, USA, pp. 88-97.

[25]   Crossbow Technology Inc., 1421 McCarthy Boulevard, Milpitas CA 95035

[26]   Evans, R. and Bergman, J., 2007, "Relationships between cropping sequences and irrigation frequency under self – propelled irrigation systems in the northern great plains," USDA annual report, Project number: 5436-13210-003-02.

[27]   Jennifer Yick, Biswanath Mukherjee and Dipak Ghosal, 2008, "Wireless sensor network survey," Computer Networks 52, 2292-2330.

[28]   Ratkowski J., 1961, "Experiments with galloping spans," AIEE Winter General Meeting New York, N.Y., paper 62.

[29]   Alonso, G., Meseguer, J. and Pérez-Grande, I., 2005, "Galloping instabilities of two-dimensional triangular cross-section bodies", Experiments in Fluids, 38, pp. 789-795.

[30]   Alonso, G. and Meseguer, J., 2006, "A parametric study of galloping of two dimensional triangular cross section bodies", Journal of Wind engineering and Industrial Aerodynamics, 94, pp. 241-253.

[31]   Lee, P C Y., 1991, "A Variational Principle for the Equations of Piezoelectromagnetism in Elastic Dielectric Crystals", Journal of Applied Physics, 69(11), pp. 7470.

[32]   Nisse, E P E., 1967, "Variational Method for Electroelastic Vibration Analysis", IEEE Transactions on Sonics and Ultrasonics, Vol. SU-14(4), pp. 153.

[33]   IEEE Standard on Piezoelectricity, ANSI/IEEE, Std. 176, 1987.

[34]   Matlab Simulink, Mathworks.

[35]   Product Information, 2010, Piezo Systems Inc., 65 Tower Office Park, Woburn, MA 01801, USA. http://www.piezo.com/prodsheet2sq5H.html

[36]   Analog   devices,   USA.   http://www.analog.com/en/sensors/inertial-sensors/adxl322/products/product.html

[37]   Schwartz, M. N., and Elliot, D. L., 1993, "United States Areal Wind Resource Assessment", Report PNL-SA-21606, Presented at the Alternate Fuels and the Environment Symposium, Denver, CO.

VITA

Rohan Ram Mahadik was born in Ratnagiri, India. After completing his study in schools at Mumbai and Ahmedabad, India, he entered Nirma University in Ahmedabad, India. He received the degree of Bachelor of Technology in Mechanical Engineering from Nirma University in June, 2007. During the following year, he was employed as Member, Research and Development, Chassis-Suspension, at TVS Motor Company in Bangalore, India. In September, 2008, he entered the Graduate School in Aerospace engineering at the University of Texas at Austin.

Permanent email: rohanez@gmail.com

Permanent Address: 203 Kirtankunj, Champaner Society,

Usmanpura, Ashram Road,

Ahmedabad-380013

India

This thesis was typed by the author.